

Observing the Sun from start to finish: The Tunable magnetograph's design, calibration, data reduction and scientific exploitation.

PhD dissertation by

Pablo Santamarina Guerrero

Instituto de Astrofísica de Andalucía (IAA-CSIC)

Programa de Doctorado en Física y Matemáticas (FisyMat)
Universidad de Granada

A thesis submitted in fulfillment
of the requirements of the degree of
Doctor of Philosophy

October 9, 2024

PhD thesis supervised by

Dr. David Orozco Suárez

Dr. Julián Blanco Rodríguez



INSTITUTO DE
ASTROFÍSICA DE
ANDALUCÍA



EXCELENCIA
SEVERO
OCHOA



UNIVERSIDAD
DE GRANADA

CONTENTS

1	Introduction	3
1.1	Background	3
1.2	Motivation of our work	4
1.3	Introduction	6
1.4	A brief introduction to spectropolarimeters.	7
1.4.1	Imaging and optical quality.	7
1.4.2	Spectroscopy	13
1.4.3	Polarimetry	13
1.4.4	What do spectrpolarimeters tell us about the Sun?	16
2	Sunrise III and TuMag: Design and calibration.	19
2.1	Sunrise III	20
2.1.1	Observatory's design	21
2.1.2	Science with Sunrise.	22
2.2	The Tunable magnetograph: TuMag	24
2.2.1	TuMag's design and light path.	24
2.2.2	Instrument performance and verification.	26
2.2.2.1	Imaging performance.	27
2.2.2.2	Spectral performance.	29
2.2.2.3	Polarimetric performance.	33
3	TuMag's pipeline and data.	37
3.1	TuMag's observing modes	38
3.1.1	Calibration modes	40
3.1.1.1	Flat-field observations	40
3.1.1.2	Dark-current observations	41
3.1.1.3	Linear polarizer and micropolarizers observations.	41
3.1.1.4	Pinhole Observations.	42
3.1.1.5	Straylight target.	42
3.1.1.6	Prefilter scans.	42
3.1.1.7	Phase diversity.	43
3.2	Timelines	43
3.3	Pipeline	47

3.3.1	Standard data reduction process.	47
3.3.2	Extra calibration blocks.	50

rals for page numbers

CHAPTER 1

INTRODUCTION

1.1 Background

In June 2009, the first Sunrise observatory (Barthol et al., 2011) was launched from Kiruna, Sweden, aboard a stratospheric balloon. Equipped with a 1-m aperture telescope, a multi-wavelength UV filter imager, and IMaX, a Fabry-Pérot-based magnetograph, Sunrise was the most complex payload carried by a solar stratospheric balloon to date. Aimed at studying the magnetic fields of the Sun and the dynamics of solar plasma convective flows, the mission was an outstanding success. It resulted in the publication of over a hundred peer-reviewed scientific articles in numerous high-impact journals, including *Astronomy and Astrophysics* (A&A), *The Astrophysical Journal* (APJ), and *Solar Physics*, among others.

Following the success of its inaugural flight, Sunrise embarked on a second journey (Solanki et al., 2017) on June 13, 2013. The primary objective of this subsequent flight was to investigate the active regions of the Sun, as it remained completely *quiet* throughout the entirety of the initial flight. Despite minimal alterations to the instrumentation aboard the observatory, the variance in solar activity during this second flight yielded fresh perspectives and valuable data, ultimately securing the mission success, despite encountering some technical challenges.

Given the success of the first two flights, a third iteration of the Sunrise mission was planned, featuring an updated design. For this third edition, the telescope was equipped with three post-focal instruments: SUSI, a UV spectrograph; SCIP, an infrared spectrograph; and TuMag, the evolution of the IMaX magnetograph. Sunrise III was initially scheduled to fly during the summer of 2020 but was postponed to 2022.

The third launch of Sunrise plays a crucial role in this dissertation. This thesis, initiated in 2020, was centered on the development of the data reduction pipeline for the TuMag instrument, which was entirely developed by the Spanish solar physics consortium. According to the original plan, the first half of the thesis was dedicated to the calibration of the instrument and the preparation of the data pipeline. This way, once the mission was launched, the second half of the thesis could focus on the correction and scientific analysis of the data produced during this third flight. However, this plan (and thus the scope of the thesis) encountered a setback on July 10, 2022, when the third flight of the Sunrise observatory had to be aborted just a few hours after the launch due to a mechanical failure during

the ascent phase.

The observatory was recovered days later after a brief stay in the Scandinavian Alps. Both the telescope and the instruments were found to be in good condition, allowing for the recovery of the observatory and providing hope for a second attempt. However, the process of retrieving the instruments, disassembling, calibrating, and verifying their condition before relaunching the mission is lengthy, and it was not until this year, 2024, that a second attempt became feasible.

In the absence of data produced by Sunrise to process, analyze, and exploit, the scientific work conducted within the framework of this thesis has been compelled to slightly shift its focus. Over these years, we have focused on delving deeper into image correction techniques for data obtained from Fabry-Pérot interferometers, such as TuMag and IMaX. As well as conducting several studies using data products from other instruments, such as the Polarimetric and Helioseismic Imager aboard Solar Orbiter (SO/PHI) and HMI.

It wasn't until the 10th of July of 2024 that Sunrise III got its second chance to fly, and this time, the opportunity was not wasted. After a very successful flight that lasted 6 days, the observatory landed in the northern region of Canada on the 16th of July. Figure 1.1 shows the trajectory our favourite solar observatory followed over these days. The recovery process started immediately after landing, and we were able to lay hands on the data for the first time on September 2024.

In the following chapters, we will present the work undertaken during the calibration and commissioning of TuMag, conducted in 2021, 2022, and 2024. Additionally, the research carried out between the first and second flights of Sunrise III, which has resulted in the publication of two articles as the main author — one published in APJ and the other in A&A — will also be detailed in this manuscript, as well as other studies that have not yet been published in any scientific journal.

1.2 Motivation of our work

In experimental sciences, there is a very strong relation between technological and scientific advances due to the simple fact that we cannot draw conclusions from what we cannot see. We believe it is important for experimental scientists, and more specifically, for observational astronomers, to know the limitations and capabilities and understand the functioning of the instruments we use.

This philosophy is one of the pillars of this thesis, which covers topics ranging from the design and calibration of scientific instruments to the exploitation of the data they produce. With this thesis, we aim to provide a broad, yet detailed, view of the various stages of a scientific mission, from its conception and objectives through its design and calibration, data reduction and preparation for scientific exploitation, and finally, the studies and conclusions derived from it.

In particular, we will detail this process within the framework of solar physics through the development of TuMag, the magnetograph aboard Sunrise III. We will present the scientific objectives of the mission and attempt to link the design concepts with the scientific

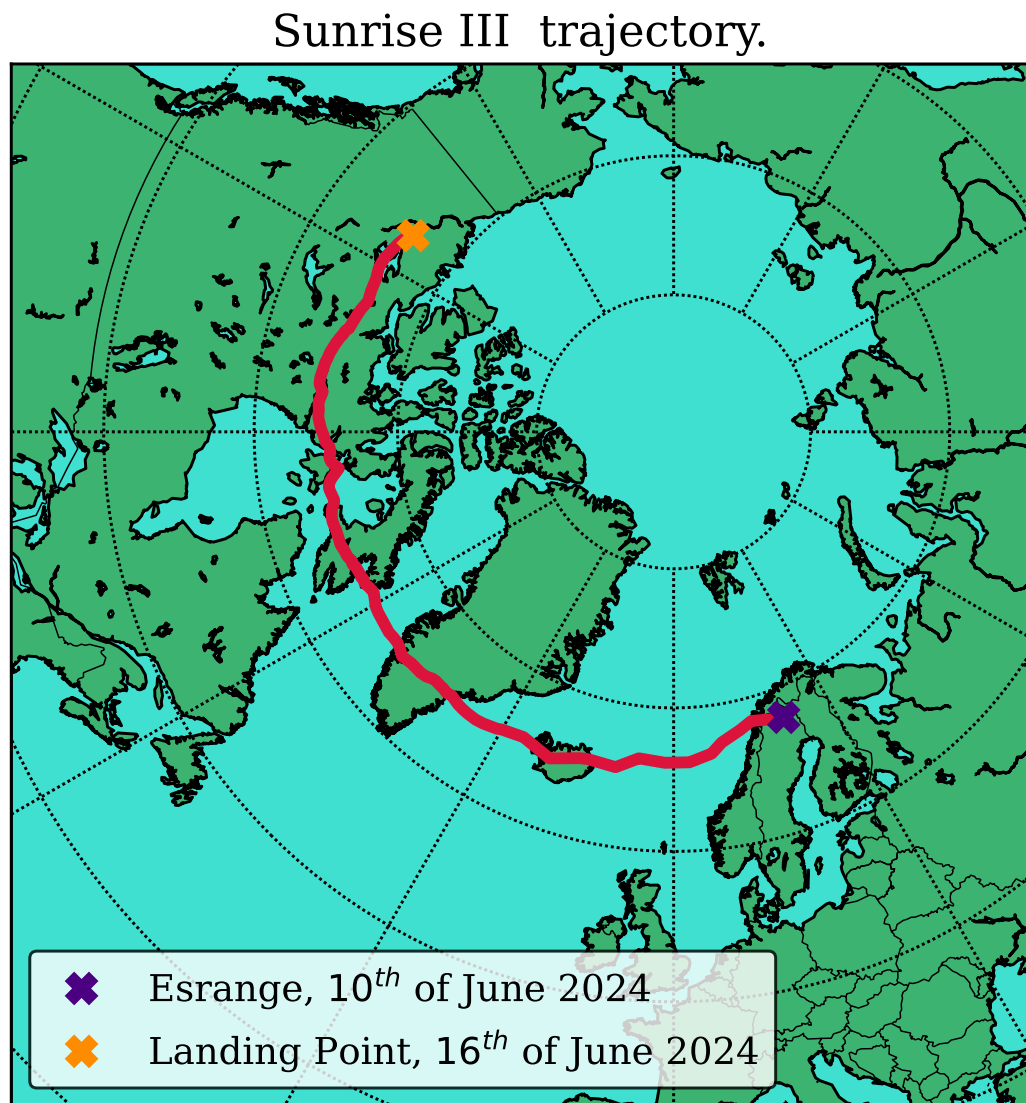


Figure 1.1 Sunrise III trajectory. Aqui poner tambien un foto de sunrise con el globo.

questions we aim to answer. We will address the challenges encountered in data correction due to the technical or instrumental limitations, a subject of ongoing debate within the community and of current relevance. And finally, we also aim to offer a brief dip into the scientific exploitation that can be carried out with the final data product.

With this thesis we aim to clarify the following points:

- ✿ Scientific objectives of TuMag.
- ✿ Instrumental ways of achieving the scientific purposes
- ✿ Open problems for data reduction. Flat-fields, etalon effects in the data.
- ✿ Offering an example of data exploitation with a study case. Persistent Homology.

1.3 Introduction

Intro general de la tesis.

Astronomy is one of the broadest fields of knowledge. It studies everything from the smallest astronomical objects, such as the small asteroids that inhabit our solar system, to the global structure and evolution of the universe, including the study of planetary systems, stars, black holes and the galaxies in which they are found. However, despite the diversity of disciplines—ranging from stellar astronomy, radio astronomy, and cosmology, to extragalactic astronomy, astrobiology, and solar physics—they all share a common tool for studying the cosmos: light. Since the very beginning of astronomy, the astronomer's work has been to learn how to modify and measure the properties of the photons that reach us in order to infer the characteristics of the observed object. Although recent advancements have provided astronomers with new lenses to *see* the cosmos, like gravitational waves (**REFERENCIA**) or neutrinos (**REFERENCIA**), among others, light remains as our main resource. Our understanding of the cosmos has always gone hand-in-hand with our ability to design and develop new (or more efficient) and clever ways to dissect the light, spanning from the first solar clocks, passing through Newton's first telescope to the modern-day spaceborne telescopes like the Hubble, James Webb or Solar Orbiter.

Solar physics is no different from other astronomical disciplines in this regard. Our main tool to *see* the Sun is through light. Contrary to what one may think, solar physicists are as photon-starved as any other astronomer. Even though our star is closer and (apparently) brighter than any other astronomical object, our requirements regarding resolution and sensitivity are so high that we are as dependent on extremely optimized instrumentation as any other discipline. Thus, the development of instrumentation employing state-of-the-art technology and techniques plays an important role in modern solar physics.

1.4 A brief introduction to spectropolarimeters.

As suggested by the name, spectropolarimeters are instruments designed to measure both the spectral and polarimetric properties of light. In other words, they assess the polarization state of light as a function of wavelength. Their use is widely extended in astrophysics, owing to the substantial amount of information that can be inferred about the light source from these properties.

There are two distinct types of spectropolarimeters, distinguished by their approach to spectroscopy: slit-based spectrographs and narrow-band tunable filtergraphs. The latter preserve spatial resolution by capturing two-dimensional images of the solar scene at the expense of sacrificing spectral resolution. Conversely, slit-based spectrographs provide excellent spectral resolution but have a limited spatial resolution.

Regardless of the method employed for spectroscopy, spectropolarimeters must be able to measure the polarization state of light, in other words, they must determine the Stokes parameters of the incident light. These four parameters, typically expressed as a pseudo-vector, $[I, Q, U, V]$, were introduced by Stokes (Stokes, 1851) as a formalism to fully describe the polarization state of light. The first parameter, I , denotes the total intensity, while Q and U provide information on the intensity of linearly polarized light at 0° and 90° , respectively. Lastly, V represents the intensity of circularly polarized light.

Outstanding polarimetric sensitivity and spectral resolution are rendered ineffective if the optical capabilities of the instrument are not up to par. The design of these instruments must achieve diffraction-limited imaging, coupled with a signal-to-noise ratio that ensures a polarimetric sensitivity for stokes Q , U and V of approximately 1000. Additionally, it must provide the best spatial resolution that the telescope allows, all while maintaining high spectral resolution and minimizing observation time. Consequently, instrument design requires a careful balance among these three properties: spectral, optical, and polarimetric capabilities.

In the following sections, we will examine each of these aspects in greater detail, with a particular emphasis on filtergraphs. Tunable filtergraphs play a significant role in this thesis, as the primary blocks of scientific work presented herein have been conducted for TuMag, a tunable magnetograph, as well as etalon-based instruments in general. Consequently, our description will be tailored to these types of instruments. It is important to note that much of the information provided will be generic and applicable also to slit-based spectrometry; however, certain specific behaviors will be unique to filtergraphs.

1.4.1 Imaging and optical quality.

Filtergraphs are, first and foremost, imagers. The high-resolution imaging that filtergraph instruments are capable of is one of the pivotal reasons for their extended use. The ability to capture a two-dimensional scene of the solar surface makes them ideal for studying solar plasma structures, which require resolutions close to 100 km on the solar photosphere. These instruments must be able to ensure an image quality and resolving power enough to measure these structures. For this reason, we will begin our description of the filtergraphs

with a brief explanation of image formation and image quality assessment.

Let us assume that the extended source we are observing has an intensity distribution in the image plane given by $O(\xi_0, \eta_0)$. Then, if we assume a linear optical system and incoherent illumination, the intensity distribution measured at a point ξ, η of the image plane is given by :

$$I_j(\xi, \eta; \lambda_s) = \iint O(\xi_0, \eta_0) S(\xi_0, \eta_0; \xi, \eta; \lambda_s) d\xi_0 d\eta_0, \quad (1.1)$$

where $S(\xi_0, \eta_0; \xi, \eta; \lambda_s)$ represents the imaging response of the instrument, also referred to as the Point Spread Function (PSF). The PSF describes the normalized intensity distribution in the image plane when observing a point source, which, due to diffraction and inherent imperfections in any imaging system, cannot be imaged as an ideal point.

The PSF is crucial in the assessment of image quality and resolving power of an instrument since it defines how fine detail will be imaged into the detector. One particularly relevant metric for image quality assessment that can be derived from the PSF is the optical transfer function (OTF), which is the Fourier transform of the PSF (Vargas Dominguez, 2009a).

$$OTF(\nu) = \hat{S}(\xi_0, \eta_0; \xi, \eta; \lambda_s), \quad (1.2)$$

where the operator $\hat{\cdot}$ is the Fourier transform, and ν represents the frequency vector in the Fourier domain.

The OTF describes how different spatial frequencies are transferred from the object to the image, thus characterizing the system's ability to resolve fine details. However, since imaging systems measure intensities, we are primarily concerned with how the intensity pattern of an object is transferred to the image. A key metric for quantifying this transfer is modulation, or contrast, which is defined as the ratio between the peaks and valleys of intensity at a given spatial frequency:

$$M_\nu = \frac{I_{max}^\nu - I_{min}^\nu}{I_{max}^\nu + I_{min}^\nu}. \quad (1.3)$$

The function that encodes the dependency of the modulation with spatial frequencies is called the modulation transfer function (MTF), and is strictly related to the OTF as the ratio of the modulation of the object MTF_{obj} and that of the image MTF_{im} can be computed from the magnitude of the OTF (Gaskill, 1978):

$$MTF = \frac{MTF_{im}(\nu)}{MTF_{obj}(\nu)} = |OTF(\nu)|. \quad (1.4)$$

From this definition, it is evident that a perfect optical system would have an $MTF = 1$ at all spatial frequencies, meaning that all details are perfectly transferred from the object to the image. However, real optical systems exhibit a decrease in MTF as spatial frequency increases. In practice, the resolution of an optical system can, and is often defined as the spatial frequency at which both the MTF and, consequently, the OTF reach zero (Tyson,

2000). This threshold frequency marks the limit beyond which the system can no longer resolve finer details.

Another key concept for assessing the imaging performance is the phase error or wavefront. The wavefront of an optical system is defined as the deviation in phase at any point within the image from that of an ideal spherical wavefront (Snyder, 1975). Such deviations arise from various optical imperfections within the imaging system, and their impact on image quality depends on the specific nature of the aberration. For instance, imperfections in mirror shape or lens configuration can result in spherical aberrations, leading to a broadening of the PSF and a subsequent reduction in resolution. Other common aberrations include astigmatism, where the focal point varies along different axes, producing distorted images, and comatic aberrations (coma), which can occur due to misalignment of optical elements and manifest as tail-like distortions in the images of point sources.

It is common to see requirements or assessment of the optical quality of optical instruments in terms of the root mean square (rms) of the variance of the wavefront, $\Delta\phi(\xi, \eta)$, usually referred to as the wavefront error (rms WFE) or simply WFE:

$$WFE = \sqrt{\frac{1}{A} \int_A (\Delta\phi(\xi, \eta))^2 d\xi d\eta}, \quad (1.5)$$

where A is the area of the aperture.

This value, essentially the standard deviation of the wavefront across the aperture, is closely tied to beam propagation quality. In fact, it can be demonstrated that the wavefront variance can be derived from the Strehl ratio, or viceversa. The Strehl ratio is defined as the ratio of the peak intensity of a point source in an aberrated system to that of an ideal system operating at the diffraction limit. It is one of the most widely used metrics for assessing the optical quality of a system, ranging from 1, for a perfect, unaberrated system, to 0. For small aberrations, the Strehl ratio (SR) and WFE are related by the following expression (Snyder, 1975):

$$SR \simeq \exp \left[- \left(\frac{2\pi WFE}{\lambda} \right)^2 \right]. \quad (1.6)$$

Although the Strehl ratio and rms WFE provide a concise measure of the optical quality of a system, the WFE contains additional information regarding imaging performance. Rather than relying solely on a single averaged value (such as the standard deviation), the wavefront can be represented as a two-dimensional map projected onto a plane normal to the light path, typically the image plane. To carry out such a representation analytically, it is essential to select an appropriate mathematical framework. Given the widespread use of circular apertures in telescopes, mirrors, lenses, and other optical components, it is advantageous to approach the problem using polar coordinates, ρ and θ , and in particular, to employ an orthonormal basis for the interpretability of the results. Among the multiple (infinite) sets of polynomials that fulfill these requirements, the Zernike polynomials (Zernike, 1934) offer some distinct advantages. The Zernike polynomials are a sequence of polynomials that compose an orthonormal basis over a unit circle. Given an arbitrary wavefront,

$(W(\rho, \theta))$, the expansion in terms of the Zernike polynomials can be expressed as:

$$W(\rho, \theta) = \sum_{n,m} C_n^m Z_n^m(\rho, \theta), \quad (1.7)$$

where Z_n^m are the Zernike polynomials, C_n^m are the amplitudes of the coefficients in the expansion and n and m are the radial order and angular frequency, respectively. The Zernike polynomials can be obtained from:

$$\left. \begin{array}{l} Z_n^m(\rho, \theta) = R_n^m(\rho) \cos(m\theta), \text{ for } m \geq 0, \\ Z_n^{-m}(\rho, \theta) = R_n^m(\rho) \sin(m\theta), \text{ for } m < 0, \end{array} \right\} \quad (1.8)$$

where $R_n^m(\rho)$ are the radial functions given by:

$$R_n^m(\rho) = \sum_{l=0}^{(n-m)/2} \frac{(-1)^l (n-l)!}{l! [\frac{1}{2}(n+m)-l]! [\frac{1}{2}(n-m)l-]!} \rho^{n-2l}. \quad (1.9)$$

This representation of the wavefront is particularly valuable because each mode, defined by a specific pair of n and m values, corresponds to a distinct aberration in the wavefront, with the associated coefficient representing the contribution to the rms WFE for that specific aberration. Furthermore, the orthogonality of the Zernike basis ensures that adding additional terms to the expansion does not influence the values of previously calculated coefficients. In other words, the Zernike polynomial expansion enables the wavefront to be expressed as the sum of individual aberrations, providing a clear decomposition of the wavefront errors.

Figure 1.2 presents an example of a simulated wavefront, including a two-dimensional cross-section and the individual Zernike components of the simulation. The simulation incorporates only the first ten Zernike polynomials, corresponding to polynomials with $n \leq 3$, which account for aberrations such as defocus, astigmatism, coma, and trefoil, among others. For a comprehensive overview of the Zernike expansion in wavefront characterization, we direct the reader to Lakshminarayanan & Fleck (2011).

Although properties such as the PSF and WFE provide us with a lot of information to evaluate the instrument's performance, they are not known a priori. Instruments need to be equipped with means to measure these quantities in order to assess the performance and correct for any defects. The strategy to follow depends on the specific characteristics of the instrument. For instance, ground-based instruments can be equipped with adaptive optics systems, where the wavefront is directly measured and corrected in real time (REFERENCES). However, this approach is not feasible for all instruments due to the technical demands required to implement such corrections. In these cases, alternative techniques, such as the phase diversity method, are necessary.

The phase diversity algorithm (Childlaw et al., 1979) is a method to infer the aberrations present in an optical system by obtaining, at least, two simultaneous, or quasi-simultaneous, images of the same object where an additional and known aberration is introduced to one of the images.

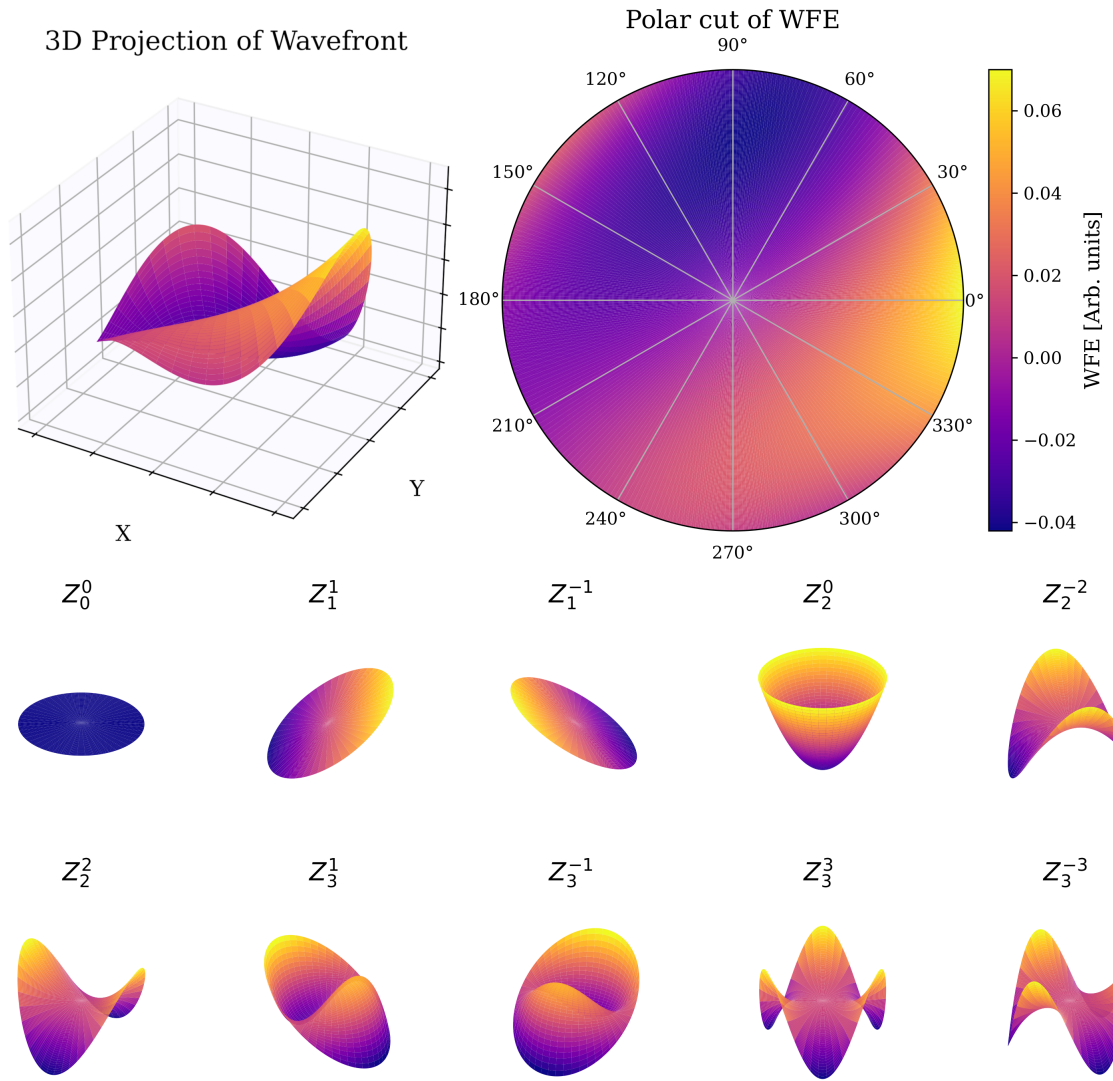


Figure 1.2 Simulation of a wavefront employing all Zernikes with $n \leq 3$. The top left panel shows the 3-dimensional representation of the wavefront and the top right panel shows a cut in a plane normal to the direction of travel. The bottom two rows show the shape of the individual Zernike polynomials included in the simulation.

The algorithm works by minimizing a cost function that depends on the OTF of the system which can be parametrized by the Zernike expansion (Paxman et al., 1992):

$$\mathcal{L}(C) = \sum_k \frac{|\hat{I}_1(\nu)\hat{S}_2(\nu, C) - \hat{I}_2(u)\hat{S}_1(\nu, C)|^2}{|\hat{S}_1(\nu, C)|^2 + |\hat{S}_2(\nu, C)|^2}, \quad (1.10)$$

where k represents the pairs of aberrated (subindex 1) and unaberrated (subindex 2) images, I stands for the intensity distributions, and S for the system's OTF expressed in terms of a Zernike expansion with coefficients C.

By finding the coefficients of the zernike expansion that minimize \mathcal{L} , we are able to characterize the wavefront and identify the aberrations present in the optical system. Thus, determining the OTF, and consequently the PSF.

Our interest in determining the wavefront and OTF is not only to evaluate the instrument's performance but also to enable image restoration by mitigating the aberrations introduced during the imaging process. The procedure for removing the effects of the aberrations consists on removing the influence of the PSF on the final intensity distribution. In other words, the goal is to *deconvolve* the PSF from the image.

Coming back to equation (1.1), we can simplify the integrals to a convolution operator assuming an spatial invariance of the PSF. In that case, the observed intensity can be expressed by:

$$I(\xi, \eta) = O(\xi, \eta) * S(\xi, \eta) + N(\xi, \eta) \quad (1.11)$$

where we added a term accounting for the noise present in real measurements $N(\xi, \eta)$.

The treatment of the problem is easier in the Fourier domain, where the convolution operator becomes a product of the fourier transforms of the corresponding functions. Therefore, in the Fourier domain, eq. 1.11 becomes:

$$\hat{I}(\nu) = \hat{O}(\nu)\hat{S}(\nu) + \hat{N}(\nu), \quad (1.12)$$

Since neither $\hat{O}(\nu)$ nor $\hat{N}(\nu)$ are known, it is not possible to analytically derive the object, even if the system's response, is known. Therefore, statistical approaches must be employed to deconvolve PSF.

One such approach is the Wiener-Helstrom filter (Helstrom, 1967), which proposes that the estimated object, \tilde{O} , can be computed as:

$$\tilde{O}(\nu) = \frac{\hat{S}^*(\nu)\hat{I}(\nu)}{|\hat{S}(\nu)|^2 + P_N(\nu)/P_O(\nu)}, \quad (1.13)$$

where the term $P_N(\nu)/P_O(\nu)$ represents the ratio between the power spectral densities of the noise and the object. Although this factor is unknown, it can be estimated based on the expected S/N in the data.

1.4.2 Spectroscopy

Among the tunable filtergraphs, Fabry-Pérot Interferometers (FPIs), also known as etalons (used interchangeably), represent one of the most prevalent forms of narrow-band tunable spectrographs. Composed by a resonant optical cavity formed by two distinct optical media, these devices allow only the passage of light with wavelengths corresponding to constructive interference within the cavity.

The transmission profile of an etalon, being produced by an interference phenomenon, is characterized by a series of narrow and periodic transmission peaks. The wavelengths at which these resonance peaks are located, their width, and their separation are determined solely by the physical properties of the etalon. In fact, it is not difficult to demonstrate (Bailén et al., 2019) that a resonant cavity produces a periodic transmission profile, with maxima occurring at a wavelength λ such that:

$$\lambda = \frac{2nd \cos \theta}{m}, \quad (1.14)$$

where n is the refractive index of the medium inside the cavity, d is the distance between the mirrors, θ is the angle of incidence of the incoming light ray and m is the interferential order ($m \in \mathbb{Z}$).

With Eq. (1.14) in mind, it is clear that an etalon allows for tuning the wavelengths of the transmission peaks by either changing the distance between the mirrors or by altering the refractive index. Although changing the angle of incidence also results in a wavelength shift, it introduces other issues, such as ghost images or profile broadening in telecentric configurations, among other effects. Consequently, the angle is not used for wavelength tuning.

To isolate a single wavelength, or a narrow band surrounding it, it is necessary to select one transmission peak, often referred to as the main order. This is typically achieved by using a pre-filter with a small bandwidth that only allows light with wavelengths near the desired measurement region to pass through. This prefilter prevents light from other interference orders than the main one, known as secondary orders, to reach the instrument.

Figure 1.3 shows a simulation of the spectral behavior of this optical setup. The order-sorting pre-filter is shown with a shaded purple area and the unaltered transmission profile of the etalon is shown in dashed lines for different values of the refractive index. In solid lines, the resulting transmission profile is shown, that is, the transmission allowed through both the pre-filter and etalon at the same time.

1.4.3 Polarimetry

A polarimeter must determine the full Stokes components of the incoming light; however, these properties cannot be directly measured, as only the intensity of light is observed, not its intrinsic characteristics. Thus, polarimeters derive the Stokes parameters, rather than measure them. In order to do so, a series of multiple, simultaneous or quasi-simultaneous observations are taken, in which the polarization state of the incoming light is systemat-

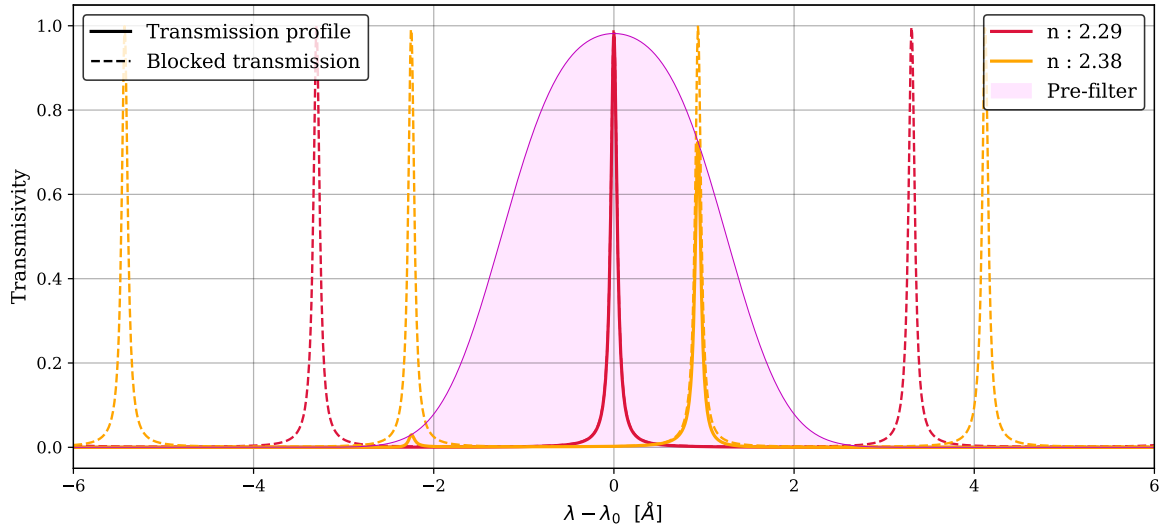


Figure 1.3 Transmission profiles of the same etalon with varying refractive indices (n). The dashed lines represent the original transmission profile, while the solid lines indicate the portion of the transmission profile that passes through the order-sorting pre-filter (shaded purple area).

ically altered. These different measurements, commonly referred to as modulations, are generated by inducing a known alteration in the polarization. The Stokes parameters are then reconstructed by combining the information from all measurements through a process known as demodulation.

In order to understand how polarimeters derive the stokes components we need to briefly model how the different modulations are generated. Mathematically, the effect on polarization of a linear and finite system can be treated as a combination of linear transformations on the Stokes vector and, therefore, can be represented by a matrix in \mathbb{R}^4 , known as the *Mueller Matrix*. Let \mathbf{M} be the matrix that describes these transformations, then the polarization state that reaches the detector follows:

$$\mathbf{I}_{out} = \mathbf{M}\mathbf{I}_{in}, \quad (1.15)$$

where \mathbf{I}_{in} and \mathbf{I}_{out} are the Stokes vectors of the light that reaches the instrument, and the detector, respectively. However, since we only measure intensities, the actual quantity measured by our CCD is:

$$I_{obs} = m_{00}I_{in} + m_{01}Q_{in} + m_{02}U_{in} + m_{03}V_{in}, \quad (1.16)$$

where m_{0i} is the i-th element of the first row of the Mueller Matrix. This means that the intensity we measure is a linear combination of the different polarization states of the incoming light. To determine the values of the individual parameters I_{in} , Q_{in} , U_{in} , and V_{in} , further independent measurements are necessary, which can be achieved by modifying the Mueller matrix. In particular, it is easy to see that four independent measurements are re-

quired in order to construct a system of equations that allows us to determine the full Stokes vector. This process is known as modulation, and the four independent measurements are the different modulations.

If we denote each of the modulations by I_j with $j \in \{1, 2, 3, 4\}$, we can construct the following system of equations:

$$\begin{pmatrix} I_1 \\ I_2 \\ I_3 \\ I_4 \end{pmatrix} = \underbrace{\begin{pmatrix} m_{01}^1 & m_{02}^1 & m_{03}^1 & m_{04}^1 \\ m_{01}^2 & m_{02}^2 & m_{03}^2 & m_{04}^2 \\ m_{01}^3 & m_{02}^3 & m_{03}^3 & m_{04}^3 \\ m_{01}^4 & m_{02}^4 & m_{03}^4 & m_{04}^4 \end{pmatrix}}_{\mathbf{O}} \begin{pmatrix} I_{in} \\ U_{in} \\ Q_{in} \\ V_{in} \end{pmatrix} \quad (1.17)$$

where the superindex in m_{oi}^j denotes the values of the Mueller Matrix for each modulation. Through straightforward algebra, it is easy to see that the stokes vector of the incoming light can be determined by $\mathbf{I}_{in} = \mathbf{D}\mathbf{I}_{obs}$, where \mathbf{D} is the demodulation matrix, the inverse of the modulation matrix, \mathbf{O} , and \mathbf{I}_{obs} is the vector containing the 4 measured modulations.

Carefully determining \mathbf{O} , and consequently \mathbf{D} , during the instrument calibration process is crucial, as the accuracy of the determination of the Stokes components depends entirely upon it. It can be proven (del Toro Iniesta & Collados, 2000) that the optimum modulation scheme—the values of \mathbf{D} that enable the Stokes vector to be computed with minimal uncertainty—satisfies the conditions:

$$\varepsilon_1 \leq 1, \text{ and } \sum_{i=2}^4 \varepsilon_i^2 \leq 1, \quad (1.18)$$

where the polarimetric efficiencies for each stokes parameter ($i = 1, 2, 3, 4$), ε_i , are defined as:

$$\varepsilon_i = \left(N_p \sum_{j=1}^{N_p} D_{i,j}^2 \right)^{-1/2}, \quad (1.19)$$

where N_p is the number of independend modulations.

When designing the modulation scheme for a given instrument, it is essential to satisfy the efficiency conditions given in Equation (1.18) to ensure optimal polarimetric accuracy for all Stokes components. Furthermore, for equal sensitivities in the measurements of Stokes parameters Q, U, and V, the corresponding efficiencies should all be equal, with a value of $1/\sqrt{3}$. This is a very important result beacause polarimetric efficiencies are directly related to the smallest measurable polarimetric signals, the polarimetric sensitivity—essentially the inverse of the signal-to-noise ratio (SNR). This relation can be expressed as (del Toro Iniesta & Collados, 2000):

$$\left(\frac{S}{N} \right)_i = \frac{\varepsilon_i}{\varepsilon_1} \left(\frac{S}{N} \right)_1, \quad i = 2, 3, 4. \quad (1.20)$$

From equations (1.20) and (1.18) it is clear that the sensitivities for computing Stokes Q, U, and V will always be lower than that of Stokes I, as their corresponding efficiencies are

smaller. To achieve an SNR of 10^3 in Stokes measurements, which is the sensitivity required to detect weak polarization signals, an SNR of at least $(S/N)_0 \gtrsim 1700$ is necessary in the measurement of Stokes I for a quasi-optimal modulation scheme.

Spectropolarimeters ultimately combine measurements in polarization, spectral, and spatial (image) domains. Consequently, the final observed intensity depends on all three properties simultaneously. By integrating the spectral behavior of the etalon and pre-filter with the polarimetric measurements, and taking into account the spatial dependence of these measurements, we can revisit equation (1.1) and rewrite it for FPI-based spectropolarimeters. In that case, the observed intensity for a modulation j at any point of the focal plane η, ξ when the etalon is tuned at a wavelength λ_s is determined by:

$$I_j(\xi, \eta; \lambda_s) = g(\xi, \eta) \int_0^\infty T(\lambda) \iint O_j(\xi_0, \eta_0; \lambda) S(\xi_0, \eta_0; \xi, \eta; \lambda - \lambda_s) d\xi_0 d\eta_0 d\lambda, \quad (1.21)$$

where $T(\lambda)$ accounts for the presence of the order-sorting pre-filter, $S(\xi_0, \eta_0; \xi, \eta; \lambda - \lambda_s)$ accounts for the imaging response of the instrument when the etalon is tuned at the wavelength λ_s , $g(\xi, \eta)$ represents a spatial gain factor that accounts for any wavelength independent pixel-to-pixel intensity fluctuations occurring in the focal plane, and $O_j(\xi_0, \eta_0; \lambda)$ is the intensity distribution of the incoming light for a modulation j and is given by:

$$O_j(\xi_0, \eta_0; \lambda) = m_{00}^j I_{in}(\xi_0, \eta_0; \lambda) + m_{01}^j Q_{in}(\xi_0, \eta_0; \lambda) + m_{02}^j U_{in}(\xi_0, \eta_0; \lambda) + m_{03}^j V_{in}(\xi_0, \eta_0; \lambda) \quad (1.22)$$

1.4.4 What do spectrpolarimeters tell us about the Sun?

Spectropolarimeters are often referred to as magnetographs (e.g., TuMag), suggesting they measure magnetic fields directly. However, this is not entirely accurate. In astrophysics, the physical properties of the light source are inferred by correlating them with the observed properties of the light, rather than measuring them directly. By evaluating the polarization of sunlight at different wavelengths, spectropolarimeters enable us to infer the magnetic field and estimate plasma velocities on the solar surface.

The simplest calculation we can carry out that provides us with physical quantities of the Sun is that of the line-of-sight (LOS) velocities. Given the spectral shift of a specific absorption or emission spectral line, $\Delta\lambda$, with respect to its rest position, λ_0 , the LOS velocities can be computed with the Doppler formula:

$$v_{\text{LOS}} = \frac{\Delta\lambda}{\lambda_0} c, \quad (1.23)$$

where c stands for the speed of light in vacuum.

The polarization properties of light come into play when determining the magnetic fields. Due to Zeeman and Hanle effects, the polarity and spetcroscopy of spectral lines can be altered when formed in the presence of magnetic fields. Due to the Zeeman effect, the spectral lines widen or split into different polarized components when a strong magnetic

field is present (del Toro Iniesta, 2003), such as in the surroundings of sunspots and active regions. In the other hand, the Hanle effect is sensitive to weaker fields, and can be used to study, for example, the magnetic structure of solar prominences or turbulent fields in the solar photosphere (Bianda et al., 1998) where the fields are not strong enough to leave an imprint through the Zeeman effect.

One simple strategy to employ polarization and spectral data to derive the magnetic fields is through the center-of-gravity method. According to Uitenbroek (2003), the LOS strength of the magnetic field can be obtained through:

$$B_{\text{LOS}} = \frac{\lambda_+ - \lambda_-}{2} \frac{4\pi mc}{eg_L \lambda^2} , \quad (1.24)$$

where m and e are the electron mass and charge respectively, g_L stands for the Landé factor and λ_+ and λ_- are the centroids of the right and left circularly polarized line components, respectively, and are computed by:

$$\lambda_{\pm} = \frac{\int \lambda [I_{\text{cont}} - (I \pm V)] d\lambda}{\int [I_{\text{cont}} - (I \pm V)] d\lambda} , \quad (1.25)$$

where the subindex "cont" stands for the wavelength at the continuum.

The vector magnetic field (*i.e.*, strength, azimuth and inclination), and not only the LOS strength can also be derived. However, the derivation of these quantities has to be achieved through inversions of the radiative transfer equation (RTE). The applicability of the different methods to carry out this inversion is an extensive topic as there are some assumptions that can be applied in some cases but not in others, such as the weak-field or Milne-Eddington approximations, among others. For an extended discussion of this topic, we refer the interested reader to del Toro Iniesta & Ruiz Cobo (2016).

CHAPTER 2

SUNRISE III AND TUMAG: DESIGN AND CALIBRATION.

Observing the Sun with the highest possible quality and resolution is crucial for deepening our understanding of the physical processes governing its behavior. This necessity drives the continuous development of new state-of-the-art observatories and advanced instrumentation. Each new instrument or telescope builds upon the technical achievements of its predecessors, integrating past knowledge while introducing innovations that push the boundaries of solar observation.

An example of such advancements is the third edition of the Sunrise observatory, which marks the culmination of a collaborative effort among several international institutions. Spearheaded by the Max Planck Institute for Solar System Research (MPS) in Göttingen, Germany, the international consortium is also composed by the Spanish Solar Space Consortium (S³PC), the National Astronomical Observatory of Japan (NAOJ), the Kiepenheuer Institute for Solar Physics (KIS) in Freiburg, Germany, and the Johns Hopkins University Applied Physics Laboratory (APL) in the United States.

Following an initial unsuccessful flight in 2022, which was aborted six hours after launch, Sunrise III was granted a second opportunity in the summer of 2024. On July 10th, 2024, at 04:22:40 UTC, the observatory was successfully launched by the Columbia Scientific Balloon facility (CSBF-NASA) from Esrange, a scientific facility operated by the Swedish Space Corporation in Kiruna, Sweden. After reaching a stable altitude of 37.5 km, the commissioning phase began, marking the official start of the observation campaign. Observations commenced shortly thereafter and continued until the campaign concluded on July 16th at 18:20:54 UTC, when the flight was terminated.

Among the payload instruments aboard Sunrise III, TuMag holds particular significance for this thesis. TuMag, an imaging magnetograph developed by the Spanish Solar Space Consortium (S³PC) under the leadership of the Instituto de Astrofísica de Andalucía (IAA-CSIC) in Granada. The S³PC also includes the Instituto Nacional de Técnica Aeroespacial (INTA), the Instituto de la Riva (IDR-UPM) at the Universidad Politécnica de Madrid, the Universitat de València (UV), and the Instituto de Astrofísica de Canarias (IAC). TuMag is central to this thesis, as the core of the work focuses on its calibration, operations, and data reduction processes.

In this chapter, we present an overview of the Sunrise III mission, with a particular focus on the Tunable Magnetograph (TuMag). We will first outline the scientific motivations behind its development and the design choices. This will be followed by a detailed discussion of the technical specifications of both the mission and TuMag.

2.1 Sunrise III

Equipped with a telescope with a 1m aperture, two slit-based spectropolarimeters and an imaging magnetograph, the Sunrise III observatory is the most complex solar telescope to ever leave the ground. The coordination of three different scientific instruments allows Sunrise to simultaneously perform narrow-band polarimetric imaging in the visible while carrying out spectropolarimetry in the near-UV and near-IR, from the advantageous point of observation of ~ 36 km of altitude without the annoying interference of the atmosphere's turbulence.

The three instruments aboard Sunrise III have been carefully designed to complement each other and address the scientific purposes of the mission. The Tunable Magnetograph (TuMag, REF), developed by the S³PC, carries out high-spatial-resolution imaging spectropolarimetry in the visible range of light. Able to tune to three different spectral lines, namely the highly Zeeman-sensitive iron lines at 525.02 and 525.06 nm, and the Mg I b₂ line, TuMag can probe the photosphere and low chromosphere quasi-simultaneously.

The absence of atmosphere allows the Sunrise Spectropolarimeter and Imager (SUSI, Ref), developed by MPS and NAOJ, to observe in the near-UV, performing imaging and spectropolarimetry in the range of 309-417 nm. The high polarimetric sensitivity and large number of spectral lines present in this range, many of which are sensible to the Hanle effect, allows SUSI to sample many heights in the solar atmosphere at the same time while measuring the weak magnetic fields.

In the same way that the atmosphere complicates the observations of the UV range from the ground, observations of many lines in the near-IR are also unfeasible with ground-based instruments due to the telluric contamination of the atmosphere. The Sunrise Chromospheric Infrared spectro-Polarimeter (SCIP, REF), co-developed by NAOJ and IAA-CSIC, takes advantage of the absence of atmosphere and observes two of the Ca II triplets lines. Spectropolarimetry measurements of these lines provides information of the 3-D structure of the chromosphere and its magnetic fields, derived thanks to the high zeeman sensitivity of the selected lines. Furthermore, the large number of available photons at these wavelengths ensures a high S/N and polarimetric sensitivities.

The ability to probe simultaneously the near-IR, the visible and the near-UV, performing high-resolution polarimetric imaging and spectroscopy makes Sunrise III an unique observatory, capable of studying the connection and interaction of the small-scale phenomena occurring at different layers of the solar's atmosphere with unprecedented detail and completeness.

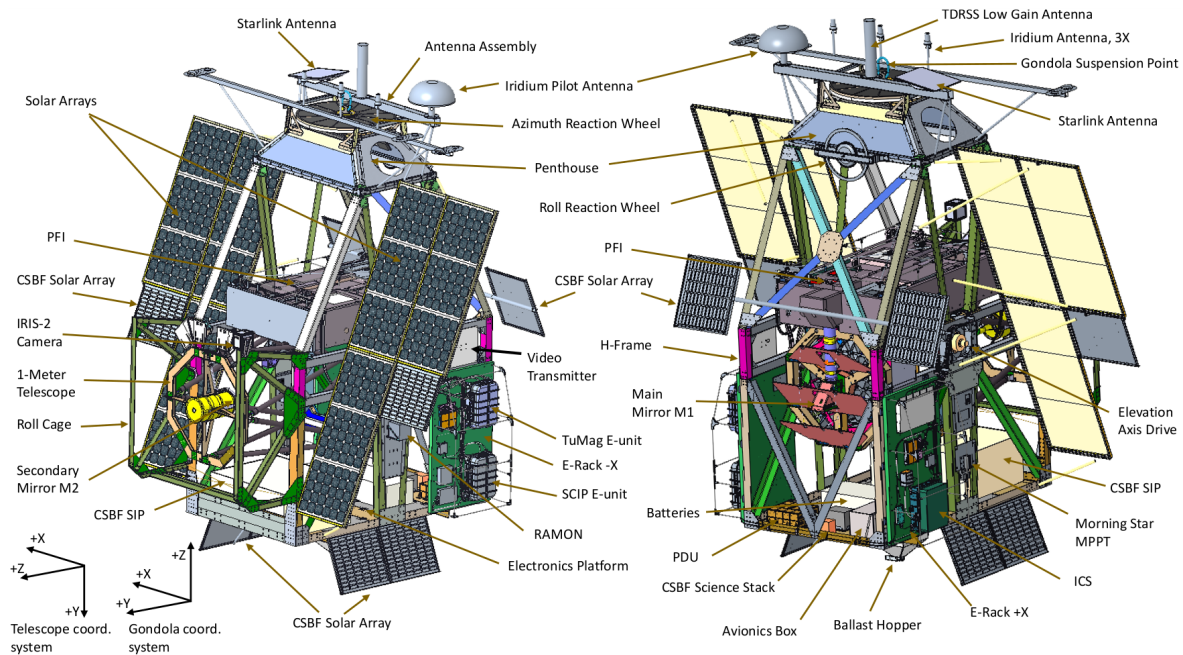


Figure 2.1 Drawing design of the Sunrise III observatory. Image reproduced from XXXXX with permission. **No he pedido permiso para esta aún, que es del paper de Sunrise III que mandó Andi, pero creo que quedaría bien algo enseñando el observatorio. Al no estar publicado el paper de Sunrise no se muy bien cual coger.**

2.1.1 Observatory's design

While the scientific instruments are central to the research performed by Sunrise, several additional subsystems play a crucial role, each contributing to the overall success of the mission.

The structural framework housing all components of the observatory, as well as the interface connecting the observatory to the flight apparatus, is provided by the gondola. This gondola, engineered by APL, is not only tasked with safeguarding the instruments and telescope during ascent and landing, but also with ensuring the stability of the pointing system. Given that the observatory is suspended from a balloon, it is subject to wind-induced motion and pendulum-like oscillations, which threaten the stability required for prolonged observations. The gondola's pointing control system (PCS) must actively counteract these disturbances in real time by making precise adjustments to the telescope's elevation and azimuth. In conjunction with the Correlating Wavefront Sensor (CWS), developed by KIS, which is responsible for image stabilization and autofocus, the PCS was required to achieve a pointing accuracy better than 0.005" root mean square (rms) over extended periods to facilitate long-duration observations.

The Sunrise III telescope is a Gregory-type reflector with a 1-meter aperture, featuring a 234 mm central obscuration and an effective focal length of 24.2 meters. This configuration provides a field of view (FoV) of 3.4', corresponding to approximately 150 Mm on the solar

surface. The telescope directs light to the post-focus instrumentation platform (PFI), located above the telescope. The PFI houses the three scientific instruments and the CWS, and is responsible for distributing light among these four instruments. This distribution, performed by the Image Stabilization and Light Distribution Unit (ISLiD), must efficiently separate the different wavelengths in a photon-efficient manner to provide the highest number of available photons to each instrument.

While all the subsystems discussed thus far directly influence the optical performance, it is equally important to recognize the crucial role played by other subsystems, such as the electronics and software control. In particular, the Instrument Control System (ICS) is responsible for the management of the observatory, gathering housekeeping and issuing commands to the electronic units of each instrument. As will be elaborated in the following chapter, Sunrise III observations were designed to operate in a semi-autonomous manner through the use of pre-programmed timelines. This approach requires that all electronic systems function in synchrony, with minimal human intervention.

2.1.2 Science with Sunrise.

The absence of Earth's atmosphere opens the window for IR and UV observations and offers a level of image stability that cannot be achieved in ground-based observatories due to atmospheric seeing. However, these advantages are also present in spaceborne missions, such as the Spectro-Polarimeter and Narrowband Filter Imager aboard the Solar Optical Telescope of the Hinode mission (Kosugi et al. 2007, Tsuneta et al. 2008), or the Polarimetric and Helioseismic Imager aboard Solar Orbiter (SO-PHI) (Solanki et al. 2020, Müller et al. 2020), among many others. Nonetheless, spaceborne missions have strong restrictions regarding payload, mass and data rate.

The absence of these restrictions in balloon-borne observatories allows for a more complex and versatile instrumentation than the one present in space missions. The combination of these two factors, namely the absence of atmosphere and the complex and advanced instrumentation they can carry, places observatories such as Sunrise in an unique position, and provides them with unique perspectives on solar phenomena.

Many aspects of the physical processes driving our Sun remain unresolved. The mechanisms underlying various solar phenomena are still the subject of debate, ranging from the origin and removal of magnetic flux in the solar photosphere to the processes responsible for heating the chromosphere and corona, as well as the small-scale dynamics of solar plasma. The three instruments aboard Sunrise work in consonance to provide novel insights into these phenomena, and aim at helping the community solve some of the open questions of solar physics.

The magnetic field, present across multiple scales and heights, is the principal driver of solar activity. Understanding the magnetic field is essential for comprehending the processes that govern solar phenomena, energy distribution, and plasma dynamics. Numerous works direct their efforts to the study of the structures and evolution of magnetic fields. For instance, several works study the emergence of magnetic flux in the photosphere, such as, Danilovic et al. (2010) and Guglielmino et al. (2012), where they utilized Sunrise I IMaX

data to examine small-scale flux emergence events occurring within solar granules. Likewise, the processes responsible for magnetic flux removal are not fully known. Several studies, such as Zwaan (1987) and Guglielmino et al. (2012), have proposed mechanisms for flux removal in the photosphere; however, no model is favoured over the other by current observations.

A thorough 3-dimensional analysis of the magnetic fields is essential to study these events. The combination of spectropolarimeters and vector magnetographs aboard Sunrise, which are capable of measuring strong magnetic fields through the Zeeman effect, and detecting weaker, more turbulent (Bellot Rubio & Orozco Suárez, 2019) magnetic fields using the Hanle effect - particularly sensible in the UV - can provide a new and complete perspective of these events.

One of the scientific targets of Sunrise is the study of the upper atmosphere, whose dynamics and heating mechanisms are not yet completely understood. In fact, the transfer of energy from the lower layers to the chromosphere and corona is one of the open problems in stellar astrophysics. Several studies propose mechanisms in which the magnetic field plays a central role in this energy transfer. Some works suggest upward currents generated by the slow motion of plasma in the photosphere as a driving mechanism (Parker (1983), Pontin & Hornig (2020)), while others highlight heating processes induced by jets (Shibata et al., 2007) or magnetic vortex phenomena, such as twisted magnetic fields known as solar tornadoes (Wedemeyer-Böhm et al., 2012).

Although some observational signatures of these processes have been detected, the detailed characterization of these events requires higher spatial and temporal resolutions than those currently available. The high-cadence UV observations, where several spectral lines sensitive to the weaker magnetic fields of the chromosphere are present, combined with magnetic field maps of the photosphere and lower chromosphere provided by TuMag, and complementary observations of the Ca II infrared lines, provide Sunrise with the necessary tools to investigate these phenomena with unprecedented detail.

Sunrise also aims to provide novel insights into small-scale plasma dynamics. The Sun is highly dynamic, with structures evolving on timescales of minutes. Several studies propose that the magnetism in the quiet Sun is driven by the turbulent small-scale dynamics of the plasma (Petrovay & Szakaly (1993), Hotta et al. (2015), Rempel et al. (2023), among others). However, investigating these processes requires high spatial and temporal resolutions, which are often unattainable in ground-based observations. Similarly, other approaches to plasma dynamics, such as helioseismology (Gizon et al., 2010), also demand such high-resolution data. To address these challenges, Sunrise III conducted extended, highly stable due to the absence of atmospheric seeing, and uninterrupted observations lasting up to 6 hours, with the highest temporal resolution permitted by the (S/N) requirements.

In addition to these objectives, Sunrise will explore new and exciting areas, including the measurement of the polarized solar spectrum in the UV. This spectral region remains largely unexplored due to the technical challenges associated with its observation. Atmospheric absorption makes it impossible to observe this band from ground-based observatories, and it has yet to be measured by any space mission. SUSI is the first UV spectropolarimeter to acquire high-resolution data in this wavelength range.

Requirements	Value
Field of view	63'' x 63''
RMS wavefront error	$W \sim \lambda/14$
Spatial sampling	3 × 3 pixels
Plate scale	0.0378'' / pixel
Polarimetric efficiencies	$\epsilon_{1,2,3} \lesssim \frac{1}{\sqrt{3}}$
SNR ratio	$(\frac{S}{N})_0 \gtrapprox 1700$
Spectral resolution	< 9 pm
Spectral lines	Fe I 5250.2 Å, Fe I 5250.6 Å and Mg I b_2 5172.7 Å.
Time for a two-line observation	< 90 s

Table 2.1 Tumag scientific requirements.

2.2 The Tunable magnetograph: TuMag

TuMag is an FPI-based tunable imaging spectropolarimeter, capable of measuring the full Stokes vector across various spectral lines. This tunability allows TuMag to probe the magnetic field in both the photosphere and lower chromosphere, with high resolving power, thanks to its near-diffraction-limited imaging capabilities. The design of TuMag is inherited from IMaX, the imaging spectropolarimeter that flew aboard previous Sunrise missions. However, TuMag incorporates several advancements over its predecessor, including the addition of filter wheels for tunability between spectral modes and calibration systems, along with newly designed cameras and modulation packages.

In this section, we present an overview of the design of TuMag and its performance. It is important to note that this discussion will primarily focus on the instrument's optical design and performance—specifically its polarimetric, spectral, and imaging properties. The thermal design and control software, while crucial to the instrument's functionality, will not be covered here to avoid excessive length. Nonetheless, it is essential to acknowledge that these aspects are integral to TuMag's overall performance and represent a substantial portion of the effort contributing to its success.

2.2.1 TuMag's design and light path.

As a polarimeter, TuMag must be able to measure the full Stokes vector of the incoming light. To achieve this, it must generate four distinct modulation states and measure them in an almost simultaneously manner. As a spectrometer, TuMag must possess the capability to select specific wavelengths along multiple spectral lines. This selection process involves, first filtering the light with a pre-filter, which selects a "broad" spectral range, followed by an etalon that further narrows the bandpass within the selected range. Throughout this procedure, stringent requirements regarding polarimetric sensitivity (efficiency), spectral resolution, and imaging quality must be maintained. A summary of these requirements is presented in Table 2.1.

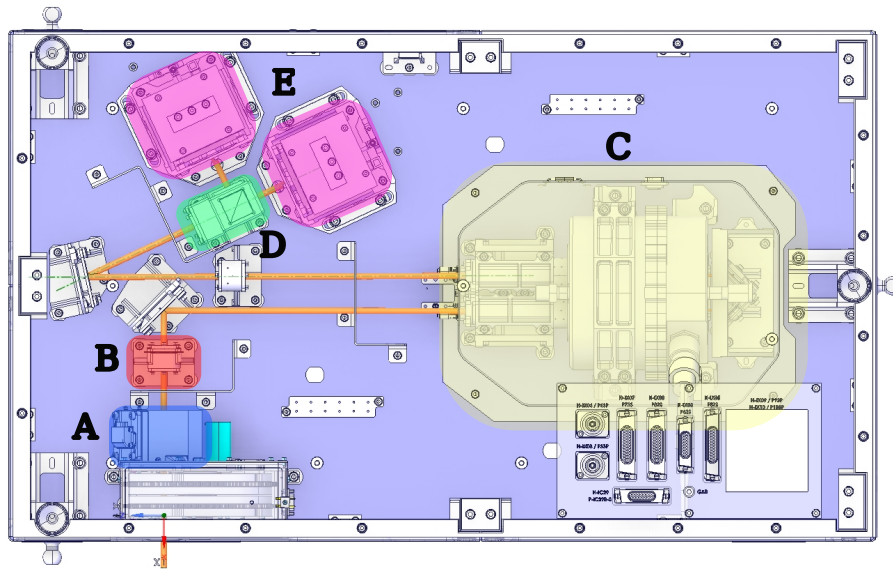


Figure 2.2 Schematic representation of the Tumag instrument. Some relevant optical devices in the light path (yellow line) are highlighted with a colored box and labeled with letters from A to E: A) Filter wheel, B) PMP, C) Etalon oven, D) beam-splitter and E) cameras. Image taken from TUMAG PAPER REF, reproduced with permission.

Light is delivered to TuMag by the ISLiD system and subsequently re-imaged onto two cameras where the images are recorded. Before reaching the cameras, the light passes through all the different subsystems of the optical unit. The first components encountered by the light are a blocking prefilter and the filter wheels (box A in Fig. 2.2). The blocking prefilter, with a wide bandpass centered at 520 nm, is employed to eliminate unwanted spectral ranges. The filter wheels are comprised by a double-disk system (Sánchez et al., 2022) that houses the prefilters for selecting specific spectral lines and a series of calibration modules. Specifically, three prefilters are mounted on the second disk of the filter wheel, corresponding to the spectral lines Fe I 5250.2 Å, Fe I 5250.6 Å, and Mg I b_2 5172.7 Å. Additionally, the filter wheels include a PD plate, which is used to introduce a known defocus into the final image to facilitate image reconstruction techniques, along with a linear polarizer, a plate of micropolarizers, and a pinhole set, employed during calibration observations.

After passing through the filter wheels, the light is directed into the Polarization Modulation Package (PMP), a subsystem derived from the SO/PHI instrument (Álvarez-Herrero et al. 2018a, Solanki et al. 2020), highlighted with the red box in Fig.2.2. The PMP's primary function is to modulate the light to produce the different polarization states required to deduce the Stokes components. This is achieved using two liquid crystal variable retarders (LCVRs), which are oriented with their fast axes at 45° relative to each other. These LCVRs induce a retardance on the transmitted light that varies with the voltage applied across the crystals. The system can operate in two distinct modulation schemes: a vector modulation scheme, which generates four independent linear combinations of equally-weighted Stokes components across consecutive observations, allowing for the retrieval of the full Stokes

vector after demodulation; and a longitudinal modulation scheme, which generates only two modulations, providing information solely on the intensity and circular polarization.

Following modulation, the light is directed into a LiNbO₃ Fabry-Pérot etalon, highlighted in yellow in Fig.2.2 (box C). Likewise IMaX, the etalon operates in a collimated setup and with a double pass configuration (Álvarez-Herrero et al., 2006). In this configuration, after the light passes through the etalon once, it is redirected by a pair of mirrors to pass through the etalon a second time. This double-pass configuration significantly enhances spectral resolution by narrowing the transmission profile. The LiNbO₃ etalon tunes the resonance wavelength by varying the refractive index of the cavity through the application of high voltages (ranging from -4000 V to 4000 V). Compared to air-gapped etalons, these kind of etalons offer the advantage of having no moving parts, which is particularly beneficial for spaceborne or balloon-borne instruments. However, this advantage comes with the need for precautions to prevent discharges caused by air ionization.

The final optical element the light encounters before reaching the cameras is a polarizing beam splitter (green box C in Fig.2.2). At this stage, the light beam is divided into two orthogonal, linearly polarized components, each directed towards a different camera. This dual-beam configuration (Lites, 1987) is designed to minimize spurious signals induced by jitter of the gondola (see del Toro Iniesta (2003) for an extended discussion), as it effectively cancels fluctuations from Stokes I to the other Stokes parameters that may arise due to image motion or solar evolution (*i.e.* cross-talk).

Light then reaches the cameras, shown with pink boxes (boxes E) in the scheme, where images from both are recorded and stored. After mission recovery, the data is processed on-ground to combine images from the different cameras, modulation states, and spectral lines, ultimately deriving the scientific products. This processing and reduction of the data is accomplished using software specifically developed for TuMag, which will be extensively discussed in Chapter 3.

2.2.2 Instrument performance and verification.

All subsystems within the TuMag light path function collaboratively to deliver high-resolution spectroscopic data of the solar spectrum. To ensure data quality, TuMag underwent multiple verification and calibration processes, during which its spectral, polarimetric, and imaging properties were meticulously tested. These procedures, commonly referred to as end-to-end (E2E) calibration tests (see Álvarez Herrero et al. (2022) for a detailed description of the tests), were conducted at various stages of the mission. Specifically, they were performed during the assembly, integration, and verification (AIV) activities with the stand-alone instrument at INTA facilities in Madrid, Spain; during the AIV phase of the PFI platform at MPS facilities in Göttingen, Germany; and during the TuMag AIV phase in the Sunrise III mission at ESRANGE facilities in Kiruna, Sweden. These tests were designed not only to validate the instrument's capabilities but also to measure critical parameters such as the tuning constant of the etalon, modulation matrices, and best-focus position—each of which is vital for the optimal operation of TuMag and the subsequent data processing. We will now delve into the details of the imaging, spectral and polarimetric properties of

the instrument as well as the verification processes and results, as the two are intimately related.

2.2.2.1 Imaging performance.

TuMag captures photons using two custom-made cameras (Orozco Suárez et al., 2023) equipped with GPIXEL back-illuminated GSENSE400BSI detectors, each featuring a $2k \times 2k$ pixel array, and specifically designed to meet TuMag's scientific requirements. These cameras provide a broad FoV of $63'' \times 63''$, sufficient to encompass an entire medium-sized active region, with a plate scale of $0.0378''/\text{pixel}$.

In order to fulfill the requirement of the wavefront error of $W \sim \lambda/14$, the instrument must have means to correct for the additional aberrations introduced by the telescope, the image stabilization and light distribution (ISLiD) system and uncorrected jittering. For this purpose, TuMag is equipped with a PD plate in the filter wheel that allows for the assessment of the PSF during the observations to apply image restoration techniques during the data processing.

The imaging E2E tests involved projecting several targets at the F4 focus, including a USAF test target, star targets, and a grid, observed both with and without the PD plate. These targets were utilized to evaluate the MTF and to assess the resolving power of TuMag. The PD measurements enabled verification of the wavefront error (WFE) derived from the MTF and an evaluation of the image quality following image restoration.

The USAF target^{*} consists on a series of horizontal and vertical line pairs (lp) arranged in sets of three with varying resolutions. Identifying the highest resolution group observable with TuMag allows for a fast diagnostic of the instrument resolution and performance. In fig. 2.3, measurements of group 4 and 5 (and higher) of the USAF target are shown for both cameras and the three pre-filters. The second set of group 5 (highlighted in a white box), which corresponds to 35.9 lp/mm in the target and 24.3 lp/mm in the image, is of special interest since its close to the Airy disk radius (26.4 lp/mm) and therefore close to TuMag's resolution limit.

The results show a better optical performance for the 517 nm pre-filter than the other two pre-filters. The USAF 5.2 set is clearly resolved fo this pre-filter in both cameras showing almost no difference between vertical and horizontal resolutions. However, results for the 525 nm prefilters exhibit a worsening of the resolution, with the same set being hardly resolved in the horizontal direction in both prefilters.

However, a more precise evaluation of the optical performance can be achieved from the MTFs. Figure 2.4 shows the MTFs computed with a slit target (see Huang et al. (2013) for a description of the MTF computation method) during the E2E tests performed in December 2021 at INTA facilities. These results agree with the diagnostic carried with the USAF tests: the 517 nm pre-filter shows a good performance in both directions, with values above the expected behaviour. Meanwhile, 525 pre-filters exhibit a large difference between different directions with an important drop in vertical resolution in both cases. This observed astigmatism is attributed to the etalon and physical deformations of the pre-filters caused by

^{*}The 1951 USAF target from Thorlabs Inc, model: R1DS1N.

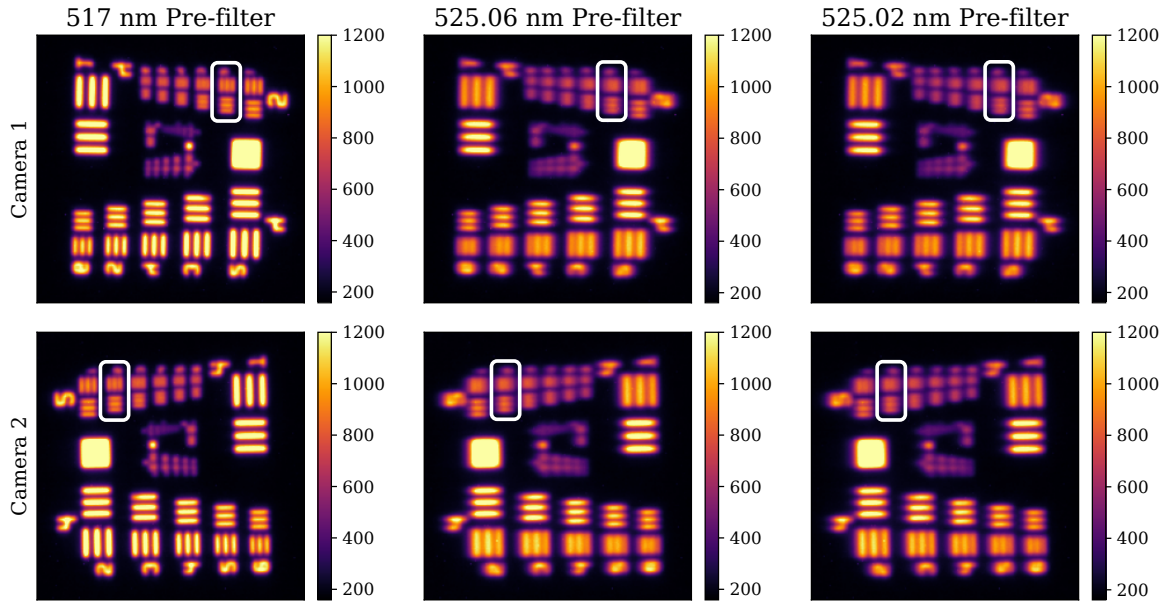


Figure 2.3 USAF target measurements for both cameras and the three pre-filters performed during E2E tests at INTA facilities on December 2021. The white boxes highlight the second element of the test group 5 (35.9 lp/mm). The scale of the images is set in digital counts.

the mechanical method used to secure and tilt them. This effect is particularly noticeable in the iron pre-filters due to the higher angles of incidence required for their tuning.

The comparison of the obtained MTF and the diffraction-limited one allows for an estimation of the Strehl ratio, and consequently the wavefront error (see section 1.4.1).

Table 2.2 shows the results for the Strehl ratios and WFE derived from this computation. All values, except for the horizontal resolution in camera 1 of the 517 nm prefilter are lower than the $\lambda/14$ set as a requirement. However, images can always be restored if $WFE \gtrsim \lambda/5$ (Vargas Dominguez, 2009b) if the PSF is known, thus the need for the inclusion of PD capabilities in the instrument. Furthermore, PD techniques not only allow us to enhance the optical performance of the instrument but also evaluate the optical performance during the calibrations in order to verify the results obtained through the computation of the MTF.

Figure 2.5 shows the measurements and results of the PD analysis for the 517 nm pre-filter and the camera 1. The measurements were carried out during the final E2E tests performed at Kiruna on April 2024 using the random dot target (left and central columns of the figure). The measurements consist on 5 sets of focused-defocused pairs of images. The PD algorithm is run over a zoomed-in region of 600 pixels in sub-patches of 128x128 pixels. The mean Zernike coefficients are shown in the top right panel, where the error has been computed as the standard deviation between different sub-patches. A 2D representation of the rms WFE is also shown in the bottom right panel.

The PD analysis indicates a small amplitude for most aberrations, with coefficients beyond Z15 approaching zero, except for the spherical aberration (Z_{11}, Z_4^0) which is the dominant contribution to the rms wfe. However, the results exhibit significant dispersion, as

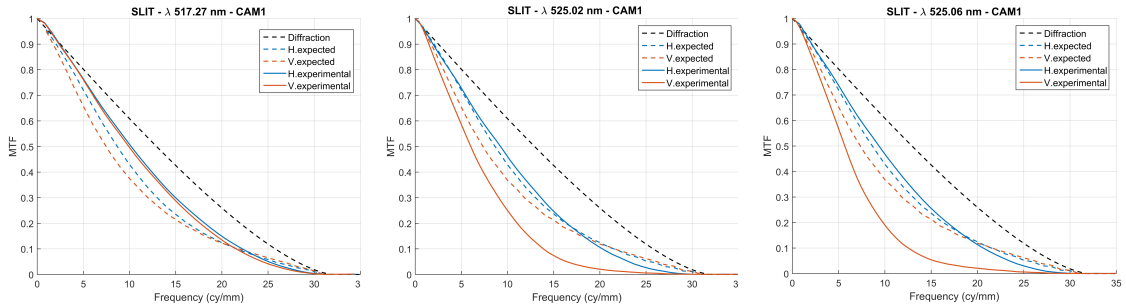


Figure 2.4 MTFs derived for camera 1 (very similar results for camera 2) for the three pre-filters from measurements of the stand-alone AIV phase performed at INTA in December 2021.

Pre-filter and camera	Strehl ratio	Strehl ratio	WFE	WFE
	Vertical	Horizontal	Vertical	Horizontal
517 nm - Cam 1	0.782	0.826	$\lambda/12.7$	$\lambda/14.5$
517 nm - Cam 2	0.761	0.806	$\lambda/12.1$	$\lambda/13.5$
525.02 nm - Cam 1	0.436	0.725	$\lambda/6.9$	$\lambda/11.1$
525.02 nm - Cam 2	0.405	0.726	$\lambda/6.6$	$\lambda/11.1$
525.06 nm - Cam 1	0.451	0.764	$\lambda/7$	$\lambda/12.1$
525.06 nm - Cam 2	0.444	0.736	$\lambda/7$	$\lambda/11.3$

Table 2.2 Optical performance evaluated from the MTFs obtained with the slit target at December 2021 E2E tests.

reflected by error bars that reach values up to 0.025λ for the first coefficients. Both the defocus and astigmatism are pretty low (Zernike indexes 4, 5 and 6, Z_2^0 , Z_2^{-2} and Z_2^2 , respectively), agreeing with the results obtained from the MTF analysis which showed a good resolution in both vertical and horizontal directions. The overall rms WFE obtained from this analysis is $\lambda/11.4$. It is important to note that the PD analysis shown here was carried out at the final stages of the calibration campaign, with TuMag mounted on the PFI and the light being fed to the instrument through the telescope and ISLiD system, whereas the MTF determination was conducted in the stand-alone AIV phase, without the aberrations introduced by these systems. Nevertheless, both analyses agree on a WFE better than $\lambda/10$, indicating very high optical quality, despite the fact that the FPI of TuMag operates in a collimated configuration, which is known to degrade optical performance (Scharmer, 2006).

2.2.2.2 Spectral performance.

TuMag filters wavelengths through a sequential process, beginning with a broad blocking pre-filter that eliminates unwanted regions of the solar spectrum, and followed by a second narrow-band pre-filter that is tuned to the three selected spectral lines. Finally, the LiNbO₃ Fabry-Pérot etalon is charged of selecting a very narrow band around specific

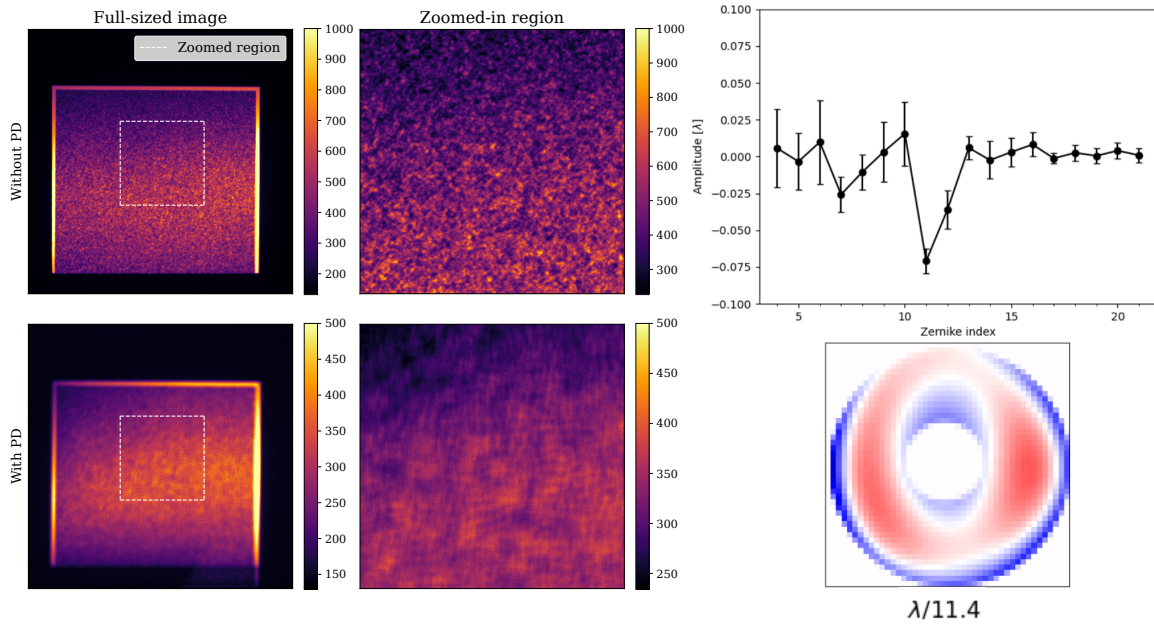


Figure 2.5 Random dot target measurements of the 517 nm pre-filter with the camera 1 and without the PD plate (left and central columns) taken during the Sunrise III AIV phase in Kiruna on April 2024. The right column shows the Zernike coefficients obtained from the PD analysis in the top panel and the 2D representation of the rms WFE. The PD analysis has been carried out by F. J. Bailén, reproduced with permission.

wavelengths along the spectral lines. The narrow-band pre-filter and the etalon are critical to TuMag's spectroscopic performance and require careful evaluation during calibration.

The three TuMag pre-filters were custom-manufactured by MaterionTM and have a full width at half maximum (FWHM) close to 1 nm. They are centered near the rest wavelength of the three spectral lines at normal incidence, with a peak transmission exceeding 80% in all cases. Each pre-filter was tuned by adjusting the incidence angle to align the peak transmission wavelength with the spectral line core. This process was performed using a coelostat at the INTA facilities, where the rest positions in volts of the spectral lines were determined. The Fe I 5250.2 Å line was found at 2129 V, the Fe I 5250.6 Å line at -2507 V, and the Mg I b_2 5172.7 Å line at -2245 V. While this tuning was successful, particularly for the iron lines, the spectral position of the pre-filters was found to be highly sensitive to illumination conditions. This sensitivity was evident from the shifts observed in the pre-filter measurements during the various stages of the assembly process. As illustrated in the left column of Fig. 2.6, the variation in the spectral position of the pre-filters is not sufficient to cause the spectral line to be blocked by the pre-filter, but it may result in the spectral line falling on the wing of the pre-filter during observations.

TuMag's etalon (see Table 2.3) operates in a collimated setup with a transmission profile with a FWHM of 0.87 pm (in the double-passs configuration), thus achieving a spectral resolution that exceeds the required 9 pm. Observations of an iodine cell illuminated with

Property	Value
Reflectivity	0.892
Thickness	281 μm
FWHM (double-pass)	0.8
Tuning Constant	3300 V/ \AA

Table 2.3 Tumag Fabry-Pérot specifications.

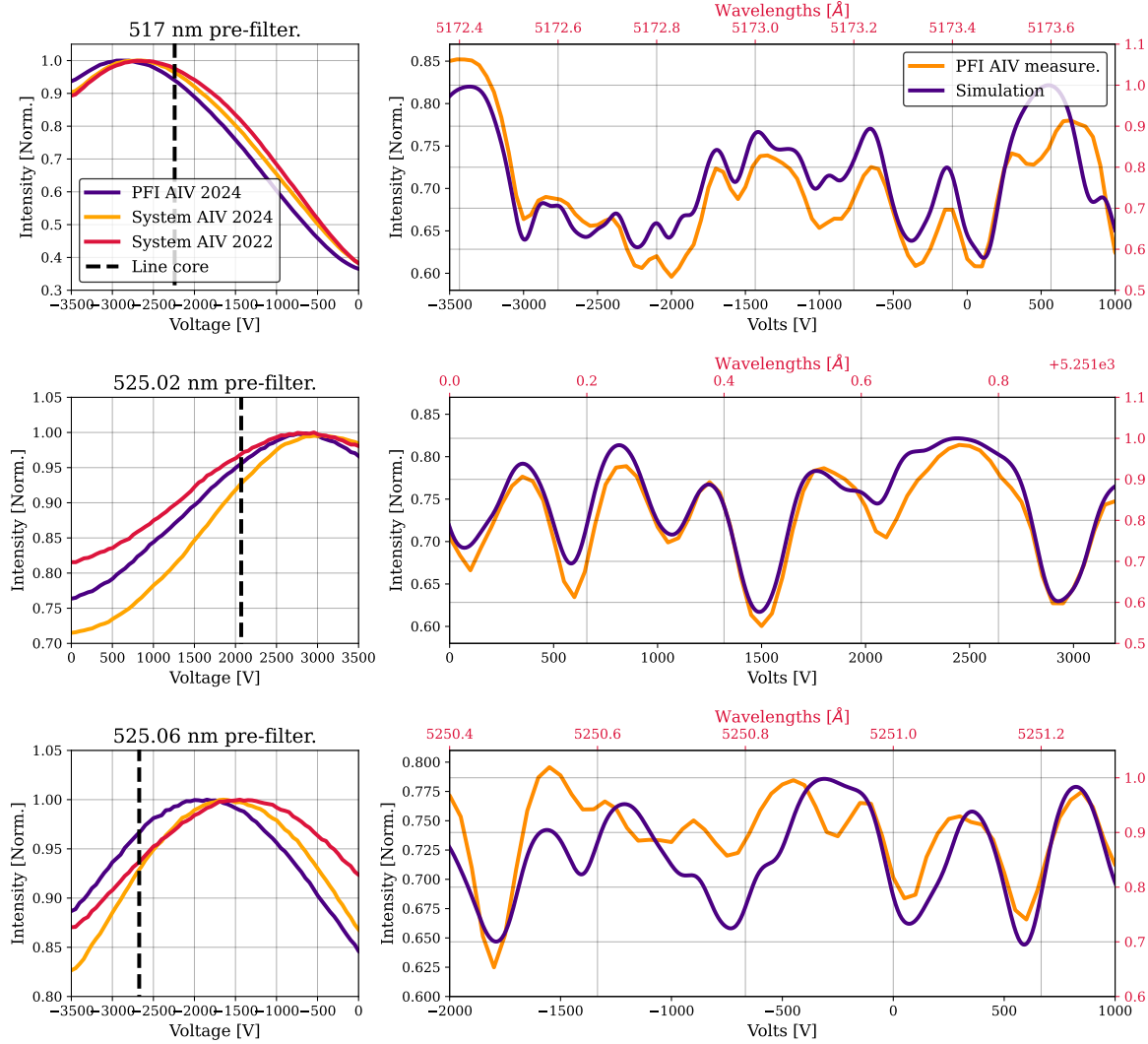


Figure 2.6 TuMag spectroscopic calibration results. Each row shows results for the 517 nm, 525.02 nm and 525.06 nm pre-filters, from top to row. The left column shows measurements of the pre-filters carried out with a flat LED on different stages of the AIV phases. The right column shows the fit of the I_2 cell observation with a simulation employing an etalon with a reflectivity of 0.892 (FWHM ~ 0.87). Note that the absolute value of the wavelengths of the simulation (red axis) might be shifted with respect to real values due to unknown conditions of the reference.

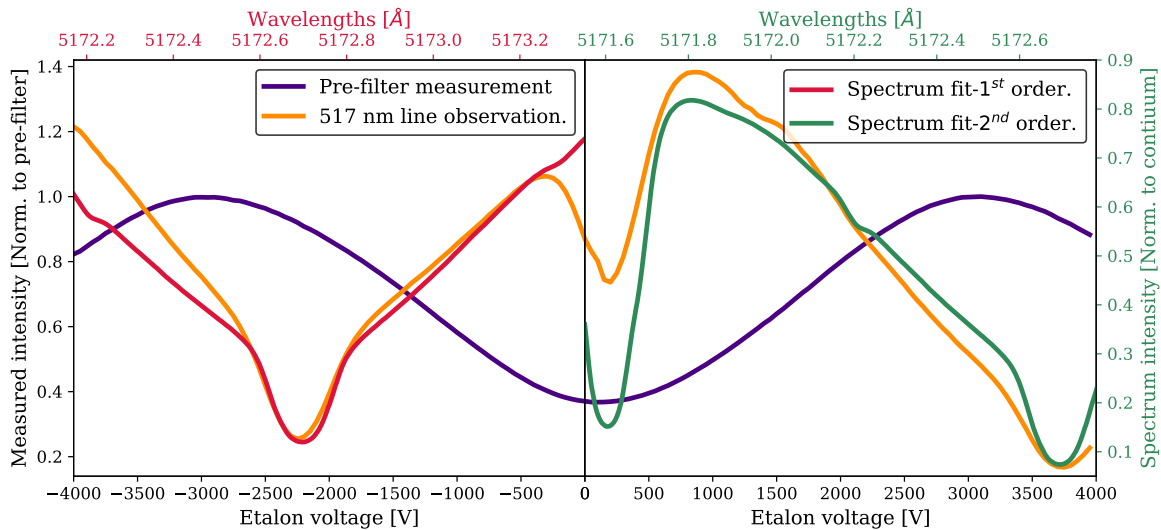


Figure 2.7 Results of the spectroscopic calibration during the end-to-end calibrations of the AIV phase of 2021. The dark blue curve represents the measurement of the 517 nm pre-filter, alongside an observation of the magnesium line using the coelostat at INTA facilities, shown in orange. Two different fits of the solar spectrum are overplotted on the figure. The red line represents a fit to the primary etalon order (negative voltages), while the green line corresponds to a fit to the second etalon order (positive voltages).

a diode were conducted to verify the transmission profile's shape and accurately assess the tuning constant. The right column of Fig. 2.6 presents, in orange, the iodine cell measurements obtained during the assembly, integration, and verification (AIV) phase of TuMag's integration into the Post Focal Instruments (PFI) platform, which took place at the Max Planck Institute for Solar System Research (MPS) in Göttingen, Germany, in November 2023. Additionally, the dark blue line in the figure represents a simulation of the iodine spectrum observations. This simulation was generated using an analytical model of the transmission profile of collimated etalons (see section ?? for a detailed overview of the model). The results confirm that the spectral resolution achieved in the iodine cell observations is consistent with the estimated 0.87 pm resolution. Furthermore, these observations enabled the calculation of the etalon's tuning constant by identifying the corresponding line cores between the simulation and observation and applying a least squares fitting to establish the relationship, which was measured in 3300 V/Å.

An observation of the solar spectrum with the 517 nm pre-filter, conducted at INTA facilities in December 2021 during the end-to-end calibration tests, is presented in Fig. 2.7, along with the corresponding pre-filter measurement. The magnesium line core is detected at approximately -2200 V using the primary order of the etalon and reappears around 3750 V with a secondary order. A fitting of the solar spectrum[†] is also shown for both orders. These results reveal significant contamination from the secondary order near the pre-filter's min-

[†]Reference

Spectral lines	Modulation	Vectorial				Longitudinal	
		I1	I2	I3	I4	I1	I2
525 & 517 nm	LCVR1 retardance	225°	225	315°	315°	180°	180°
525 & 517 nm	LCVR2 retardance	234.74°	125.26°	54.74°	305.26°	90°	270°
525 nm	LCVR1 voltage	2.291	2.533	1.992	1.947	2.761	2.761
	LCVR2 voltage	2.375	3.360	6.433	2.016	4.723	2.186
517 nm	LCVR1 voltage	2.343	2.580	2.031	1.972	2.797	2.797
	LCVR2 voltage	2.371	3.416	6.548	2.051	4.77	2.206

Table 2.4 Tumag LCVR retardances and corresponding voltages for both modulation schemes and the three pre-filters. Note that a single value is provided for both iron pre-filters.

imum transmittance. At around 0 volts, the observed spectrum (orange line) is a composite of contributions from both the primary (red line) and secondary (green line) orders. This contamination is particularly relevant for data processing, as continuum measurements of the magnesium line are typically conducted at -80 V. The broader profile of the magnesium line necessitates continuum measurements farther from the line core, making it more susceptible to this contamination. In contrast, the narrower iron lines do not require such extensive offsets for continuum measurements and are thus less affected.

2.2.2.3 Polarimetric performance.

TuMag modulates the incoming light through a PMP composed of two anti-parallel LCVRs. These devices can modify the phase retardance induced to the light that goes through them by changing the alignment of their molecules when subject to a voltage potential. Their advantages for airborne instruments lie in their lightweight and compact design, the low voltage required for operation ([0 – 10]V), and their efficiency in producing either four linearly independent modulation states for full-Stokes polarimetry or only two states for measuring the longitudinal component of the magnetic field through Stokes V. This versatility is a specific advantage of LCVRs, not found in quarter-waveplate-based PMPs (Pillet et al., 2004).

TuMag's polarimetric measurement approach is divided into the two modulation schemes already mentioned: vectorial and longitudinal. In the vectorial scheme, four linearly independent modulation states are generated in rapid succession by the PMP, enabling the calculation of the full Stokes vector. Conversely, the longitudinal approach generates only two modulation states, providing information on just two components. This modulation is designed to compute Stokes V by determining the quantities $I \pm V$.

Both modulation schemes are required to operate under an optimal modulation scheme. Such a scheme is defined by a modulation matrix with the following polarimetric efficiencies: $\epsilon_{opt} \geq [1, \frac{1}{\sqrt{3}}, \frac{1}{\sqrt{3}}, \frac{1}{\sqrt{3}}]$. The selected modulation scheme was based on the retardances outlined in Table 2.4. A thorough calibration of the liquid crystal variable retarders (LCVRs) was conducted to accurately determine the voltages necessary to produce the specified re-

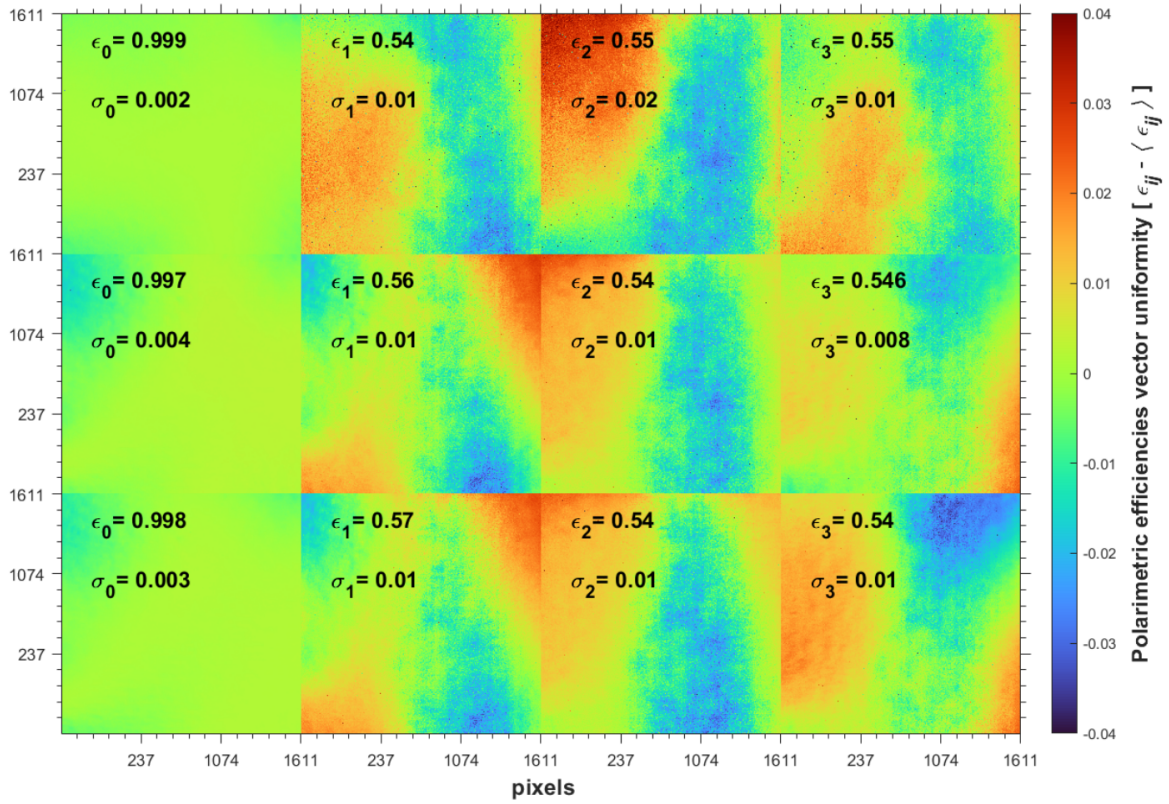


Figure 2.8 Polarimetric efficiencies for camera 1 and the three pre-filters (from top to bottom, the different rows show the results for 517 nm, 525.02 nm, and 525.06 nm). The different columns correspond to the efficiencies of the different Stokes components. The colormap measures the differences in efficiencies along the FoV. Results obtained during the E2E tests performed at INTA in December 2021, during the stand-alone AIV phase.

tardances (Álvarez-Herrero et al., 2018b).

Considerations on the (S/N) are critical for ensuring the required polarimetric sensitivity. Achieving an S/N of 10^3 in the Stokes measurements imposes a requirement of $S/N \approx 1200$ for each modulation measurement per camera. This calculation assumes near-optimal polarimetric performance, and takes into account the dual-beam polarimetry technique, which increases the S/N by a factor of $\sqrt{2}$ when combining data from the two cameras. A single shot of the cameras is insufficient to reach these S/N values, as the sensors do not have enough capacity in their electron wells. To address this, multiple exposures are captured and subsequently summed during each observation. This *accumulation* strategy, extensively tested and employed in various polarimeters (e.g., Elmore et al. 1992, Martínez Pillet et al. 1999, Lites et al. 2001), has proven compatible with image reconstruction techniques (González & Kneer, 2008; Van Noort & van der Voort, 2008). It allows for adjusting S/N levels depending on the scientific objectives of the observation, balancing between velocity and polarimetric sensitivity.

However, in order to fulfill the polarimetric sensitivity requirements, the modulation

matrix of the instrument must be carefully addressed during the polarimetric calibrations. Any deviation in the computation of the modulation matrix, will introduce spurious signals in the polarization measurements, known as cross-talk. The polarimetric calibration involves a series of measurements using a light beam with a known polarization state, generated by a rotating linear polarizer and a rotating quarter-waveplate. By varying the positions of these two devices, 40 different input polarization states were produced and measured with three pre-filters. These measurements allowed for the precise determination of the modulation matrix by solving the system of equations (1.15), where the only unknown is the modulation matrix \mathbf{M} , as both the measured modulation and the Stokes components of the incoming light are known. The modulation matrices for both cameras (indicated through the subindex) and all pre-filters that were determined through this process during the polarimetric E2E tests conducted at the Sunrise III AIV phase in Kiruna, Sweden, in 2022, are:

$$\begin{aligned} M_0^{517} &= \begin{bmatrix} 0.951 & -0.612 & 0.474 & 0.459 \\ 0.955 & -0.331 & -0.758 & -0.382 \\ 1.058 & 0.456 & 0.562 & -0.712 \\ 1.036 & 0.747 & -0.260 & 0.600 \end{bmatrix} & M_1^{517} &= \begin{bmatrix} 1.054 & 0.763 & -0.394 & -0.524 \\ 1.036 & 0.497 & 0.793 & 0.306 \\ 0.953 & -0.282 & -0.475 & 0.683 \\ 0.958 & -0.585 & 0.320 & -0.613 \end{bmatrix} \\ M_0^{525.02} &= \begin{bmatrix} 0.954 & -0.694 & 0.406 & 0.414 \\ 0.969 & -0.390 & -0.803 & -0.368 \\ 1.042 & 0.418 & 0.495 & -0.705 \\ 1.035 & 0.710 & -0.266 & 0.612 \end{bmatrix} & M_1^{525.02} &= \begin{bmatrix} 1.059 & 0.771 & -0.449 & -0.433 \\ 1.024 & 0.449 & 0.723 & 0.335 \\ 0.965 & -0.344 & -0.543 & 0.650 \\ 0.953 & -0.606 & 0.191 & -0.641 \end{bmatrix} \\ M_0^{525.06} &= \begin{bmatrix} 0.951 & -0.687 & 0.403 & 0.424 \\ 0.962 & -0.373 & -0.800 & -0.339 \\ 1.048 & 0.415 & 0.500 & -0.728 \\ 1.038 & 0.736 & -0.236 & 0.601 \end{bmatrix} & M_1^{525.06} &= \begin{bmatrix} 1.060 & 0.777 & -0.403 & -0.463 \\ 1.032 & 0.471 & 0.754 & 0.290 \\ 0.960 & -0.306 & -0.497 & 0.681 \\ 0.948 & -0.620 & 0.205 & -0.619 \end{bmatrix} \end{aligned}$$

The results of the polarimetric calibration performed during the end-to-end (E2E) tests at INTA in December 2021 are presented in Fig. 2.8. The figure shows the results for camera one; however, camera two demonstrated nearly identical efficiencies. The polarimetric efficiencies across the entire field of view (FoV) exceed the required thresholds $\varepsilon_{req} \geq [0.95, 0.45, 0.45, 0.45]$, and approach the optimal values. Furthermore, efficiency variations along the FoV are generally low, with standard deviations lower than 0.01. This homogeneity of the polarimetric performance makes the data reduction easier as no special treatment is required for specific regions.

CHAPTER 3

TUMAG'S PIPELINE AND DATA.

The 2024 observational campaign of the third edition of the Sunrise observatory was an outstanding success. In contrast to previous flights, where technical challenges severely limited the number of useful observations, all subsystems performed exceptionally well during this third flight, allowing for nearly continuous instrument operation over more than six days. From TuMag's perspective, the campaign yielded approximately 10 terabytes of data, consisting of over 40 scientific observation blocks and 250 calibration observations.

The substantial volume of data recorded by the three instruments, of which TuMag captured the least (in digital space) due to the instrument's nature, required that it be physically recovered on-site, as it could not be broadcasted from the observatory to the operations center. Recovery activities began immediately after landing and lasted until early August, during which all surviving components, along with the data vaults, were transported to Yellowknife, Canada, the nearest city to the landing site. The data vaults arrived at MPS in early August, where a backup was created before the data associated with each instrument was sent to the respective IP institution. TuMag's data arrived at IAA in late August, marking the official start of the reduction process.

The reduction process began by labeling all images and identifying the more than 600 000 images captured by TuMag. Once the observations were correctly identified, the reduction process commenced and, at the time of writing, remains ongoing. Due to the relevance of the pipeline development and results for this thesis, this chapter will provide an overview of TuMag's data and the state of its pipeline, although the results remain preliminary.

The discussion will begin by introducing TuMag's various observing modes, both scientific and calibration, followed by a brief review of the observation campaign, outlining the different observation programs and their scientific objectives. The chapter will conclude with an examination of the data reduction process, detailing the pipeline and presenting some initial results. It is important to note that, due to the late arrival of the data, this thesis had to be written in parallel with the reduction process. Therefore, the results presented here are preliminary, and the final product may differ as additional reduction steps are incorporated.

Observing mode	Spectral lines	N_λ	N_P	N_a	N_c	$t_{eff}(s)$	(S/N)
0s	Mg I b_2 5172.7 Å	12	1	2	1	6.3	500
0p	Mg I b_2 5172.7 Å	12	4	16	1	37.62	1000
1	Mg I b_2 5172.7 Å	10	4	16	1	31.81	1000
2	Fe I 5250.2 Å, Fe I 5250.6 Å	8	4	16	1	23.4	1000
3	Fe I 5250.2 Å, Fe I 5250.6 Å	5	2	20	1	10.04	1000
4	Mg I b_2 5172.7 Å	3	4	10	10	54.01	2500
5	Fe I 5250.2 Å, Fe I 5250.6 Å	3	4	10	10	53.60	2500

Table 3.1 Scientific observing modes. From left to right, the columns are: observing mode identifier, measured spectral lines, number of wavelengths, of modulations, of accumulations, of cycles, the total time and the polarimetric SNR.

3.1 TuMag's observing modes

With the purpose of simplifying the operation activities, TuMag operates through a series of so-called observing modes. The observing modes are a list of pre-configured settings tailored for various observations, including both calibration and scientific purposes. Each mode is designed to fulfill the specific objectives of the corresponding observation and enables nearly automatic operation of the instrument during flight.

A summary of the properties for each observing mode is provided in Table 3.1. There are four distinct modes designed to observe the magnesium line. Mode 0s performs a fast, extended scan of the spectral line using 12 wavelength samples: [-40, -30, -20, -10, 0, 10, 20, 30, 40, 50, 60, 65]*, with one modulation and two accumulations to maximize scanning speed. Mode 0p is similar to mode 0s but employs a full-vector modulation scheme, requiring 16 accumulations to ensure the required SNR. Mode 1 provides a shortened scan of the magnesium line, with measurements taken at [-30, -20, -10, -5, 0, 5, 10, 20, 30, 65], also utilizing a vectorial modulation scheme. Finally, mode 4 is a "deep" magnetic mode, featuring a highly reduced scan with only three samples at [-10, 0, 10], but with increased accumulations and cycles to enhance polarimetric sensitivity.

Three observing modes are configured for the iron lines. Mode 2 employs a vectorial modulation scheme applicable to both iron lines, with sampling at [-12, -8, -4, 0, 4, 8, 12, 22] pm. Mode 3 uses a longitudinal modulation scheme, measuring only Stokes I and V, with samples taken at [-8, -4, 4, 8, 22] pm. Lastly, mode 5 closely resembles mode 4, but is configured for the iron lines, with sampling at [-8, 0, 8] pm. The only difference between these two modes is the sampling scheme.

Although most of the parameters are set up by the observing mode and cannot be changed, there are some configurable parameters that allow to slightly modify the observing modes to fit the specific goal of a particular. These parameters are the following:

Solo estos? o había más?

- ✿ λ_{rep} : A parameter that allows to repeat all the observations carried out at every

*Sampling positions are given relative to the line core.

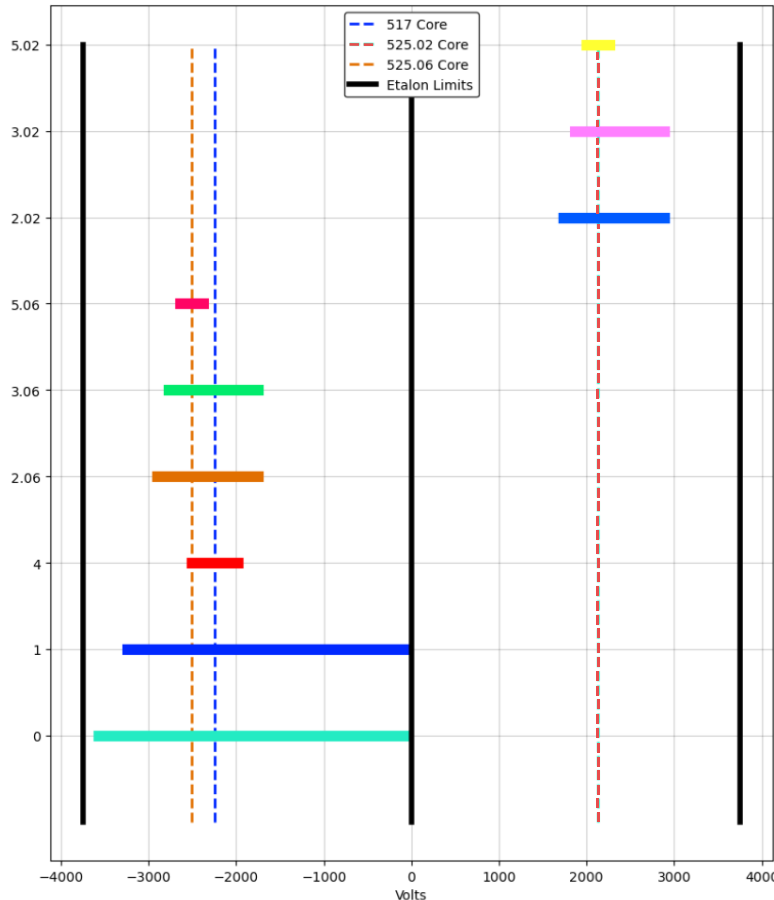


Figure 3.1 Schematic representation of the voltage range covered by all observing modes. The dashed lines indicate the position of the line core as measured during the E2E tests performed at INTA in December 2021. The black lines represent the voltage limits that cannot be crossed in an observing mode.

spectral position before changing wavelength. This parameter is employed for flat-field observations (see the following section). By default is set to 1.

- Etalon offset : A parameter that allows for the introduction of a global shift to the spectral sampling by offsetting the absolute voltages (and thus, wavelengths) of the scan. This parameter was used to center the spectral line in shorter observing modes affected by solar rotation or other effects that might shift the spectral position. The default value is set to 0 V.
- N_a : Even though the number of accumulations is fixed in nominal observing modes, this parameter was set as configurable in order to allow modifications for faster observations when needed. The default value depends on the observing mode.

Figure 3.1 presents a schematic representation of the voltage ranges for the observing modes when converting spectral sampling to volts. The black lines indicate the voltage boundaries that cannot be surpassed during an observation due to technical constraints. These limits are set at ± 3750 V as the maximum and minimum values, with an additional limitation at 0 V, since a polarity change poses technical challenges that could not be addressed within an observation mode. These restrictions are significant in two cases: firstly,

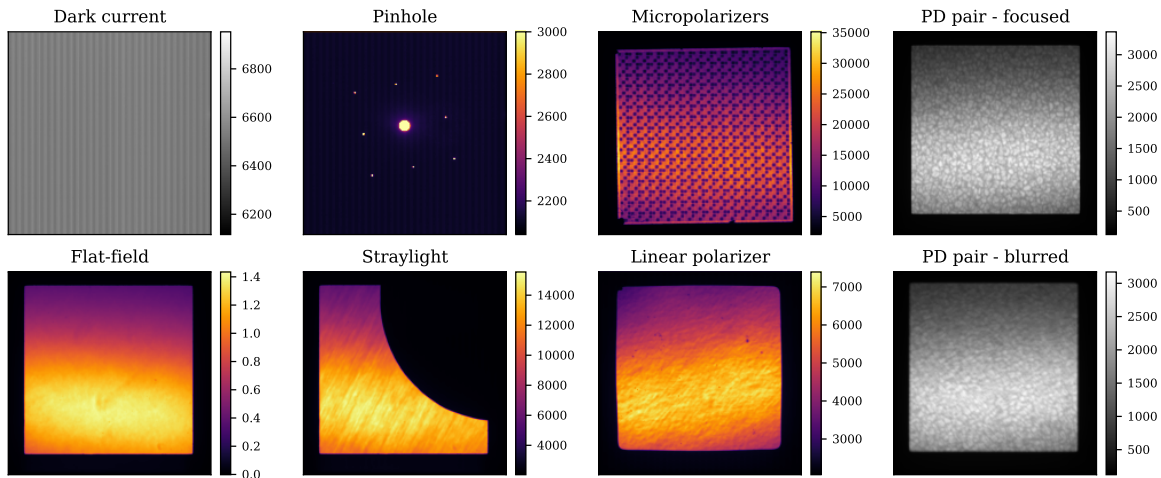


Figure 3.2 Examples of calibration observations. All images, with the exception of the flat-field, are presented in their raw format, without any manipulation or correction applied. The flat-field observation depicted corresponds to the first modulation of the continuum measurement obtained during a flat-field observation corresponding to observing mode 1. All data are belong to camera 1, and the colorbar is calibrated in digital counts save for the flat-field which is normalized to its mean value.

for Magnesium observation modes, specifically modes 1 and 0, where the continuum measurement is positioned as far from the core as possible, at -80 V, due to the 0 V crossing limitation. Secondly, these constraints are relevant when applying an etalon offset to shift the spectral positions of a particular observing mode, as the offset cannot cause the final positions to exceed these boundaries.

3.1.1 Calibration modes

An additional type of observing modes are also designed aimed at carrying out calibration observations. These calibration observing modes are more flexible than scientific ones, and allow for the configuration of several parameters to match the observations to the aim of the scientific observation.

3.1.1.1 Flat-field observations

One of the essential calibration procedures in any telescope-based astronomical observation is the acquisition of flat-field images. These observations are designed to measure intensity variations across the FoV, which arise from several factors, including intensity gradients induced by the etalon, dust particles, or pixel efficiency variations, among other sources. The aim is to capture a region with no discernible structure, ideally producing a uniformly flat intensity distribution. However, achieving such flat-field observations is not always straightforward, particularly for certain instruments. While ground-based tele-

scopes can utilize twilight periods to observe areas of the sky devoid of stars, space-borne or balloon-borne solar telescopes, such as Sunrise III, are unable to the same and must look for alternative methods.

In Sunrise III, flat-field images are generated by deliberately blurring the solar image through rapid movements of the mirror. This process effectively removes any solar structure from the FoV when averaging out multiple blurred observations, resulting in a flat-field image devoid of solar features.

In the case of TuMag, flat-field observations are performed using a modified version of the nominal observing mode, where the λ_{rep} is set to 4. Additionally, multiple consecutive instances (N_{reps}) of these observations are executed, typically 5 or 7. During data processing, a single flat-field is generated for each wavelength position and modulation state by averaging all corresponding observations.

Figure 3.2 shows an example of a flat-field observation, for one camera, modulation and wavelength (bottom left panel). The image shows a clear deviation from flatness in the measurement, primarily due to the etalon intensity gradient, which accounts for the change in intensity between the brighter bottom half and the darker top half, and some minor inhomogeneities over the FoV.

3.1.1.2 Dark-current observations

A second critical calibration procedure for any observation involving electronic cameras is the measurement of dark current. In the absence of incident photons, electrons within the camera's wells can still be randomly excited. This spontaneous excitation can be incorrectly interpreted as photon-induced counts when analyzing the data. Dark current observations are designed to characterize these random electronic excitations, which are primarily influenced by the camera's physical conditions, particularly temperature, so that they can be accurately subtracted from the final images.

For TuMag, dark current calibration involved capturing a series of 50 images with $N_a = 50$ with no light entering the instrument. As with flat-field observations, a single dark current frame for each camera is generated by averaging all individual observations. In the top left panel of fig. 3.2 a dark current shot is depicted, characterized by the vertical strips pattern.

3.1.1.3 Linear polarizer and micropolarizers observations.

TuMag's filter wheels are equipped with two targets designed to assess the instrument's polarimetric performance: a linear polarizer and a set of micropolarizers. Both targets are situated in the first filter wheel and are used in conjunction with the three distinct prefilters located in the second filter wheel. The linear polarizer serves to evaluate the polarimetric calibration, particularly by quantifying the level of cross-talk, as no circular polarization should be detected when using this target. The micropolarizers provide a more complete assessment, as they consist of multiple linear polarizers oriented at different angles.

Observations with this targets are carried with the three prefilters, at a single wavelength, located in the continuum of each line. For each measurement, a vectorial modula-

tion scheme is employed that allows for the derivation of the four stokes parameters. In the third column of figure 3.2 observations of both targets are shown.

3.1.1.4 Pinhole Observations.

Another calibration target included in the filter wheels is the pinhole target. This target blocks most of the light reaching the instrument, except for a few small holes arranged in a square-like pattern across the FoV, as shown in the top panel of the second column of figure 3.2. A larger hole is located at the center of the FoV, surrounded by eight smaller holes that trace a square with the central hole at its midpoint. These observations serve various purposes, including image alignment, detecting the presence of ghost images, or identifying etalon reflections, among other uses.

Pinhole observations are conducted similarly to those with polarizers, that is, in combination with the three prefilters at a single wavelength (the continuum of each line), but without applying any modulation.

3.1.1.5 Straylight target.

Not all the light that reaches the detector is necessarily the intended signal for a given observation. Some unwanted light, primarily originating from internal reflections along the optical path, may also reach the instrument. This unwanted contribution, known as straylight, contaminates the measurements by reducing contrast, lowering the S/N, and generally degrading the spectral, optical, and polarimetric performance of the instrument.

To address this contamination, TuMag performed a series of observations using a target that blocks part of the FoV (see the bottom panel of the second column of figure 3.2). By analyzing the dark region in these observations, it becomes possible to measure and model the straylight reaching the instrument, allowing for its subsequent removal from the data.

3.1.1.6 Prefilter scans.

TuMag observations are very sensible to spectral shifts either from the pre-filters or from the observed spectral line position. The shift of the pre-filters can happen due to changes in the physical conditions of the filter wheels such as changes in temperatures which spectrally shift the behavior of the pre-filters. The position of the pre-filter greatly affect the measurements as it reduces the intensity of the measurements that are obtained in the wings of the pre-filter. Due to solar rotation, or changes in the conditions of the etalon, although these are less likely, the spectral position at which the spectral lines are recorded can change. This effect is specially important in observing modes that require great spectral accuracy, such as the deep modes, where only three spectral positions close to the line core are employed.

In order to verify the spectral behaviour of the prefilter, as well as the position of the spectral line, a series of observations were carried out, usually before and after the scientific observations, where a spectral scan with a rich spectral smapling was taken for all the pre-filters employed in the observation. These scans, measure the voltage range of the specific line with a sampling of 100V and without modulating.

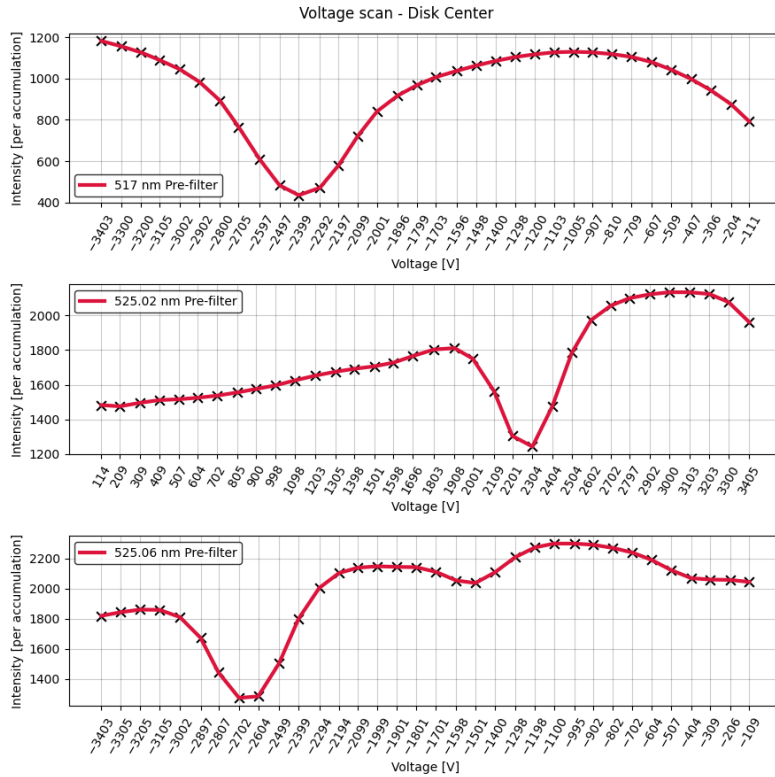


Figure 3.3 Schematic representation of the voltage range covered by all observing modes. The dashed lines indicate the position of the line core as measured during the E2E tests performed at INTA in December 2021. The black lines represent the voltage limits that cannot be crossed in an observing mode.

3.1.1.7 Phase diversity.

Lastly, TuMag is equipped with the capability to perform phase diversity for image reconstruction. As discussed in previous chapters, applying image reconstruction techniques is essential to meet the optical quality requirements. To this end, TuMag includes a PD plate in the first filter wheel that introduces a known defocus in the images. Capturing images with and without this plate enables the computation of the instrument's PSF, which can then be deconvolved from the data.

PD measurements require quasi-simultaneous pairs of aberrated and unaberrated images. Therefore, TuMag's PD observations consist of a series of 32 or 40 rapid, non-accumulated shots with the PD plate, followed by a corresponding series without the PD plate. The feasibility of this sequential scheme for phase diversity techniques has been confirmed in Bailén et al. (2022). A pair of focused-defocused images of quiet-sun observations is shown in the last column of figure 3.2.

3.2 Timelines

The operations of Sunrise III were designed to be nearly autonomous to ensure synchronization between the scientific instruments, the telescope, and the CWS. Given the limited time available for the observation campaign, this autonomy also helps to speed up operations, thus enabling more observation programs to be accommodated within the mission's

duration.

The Sun is a highly dynamic system, exhibiting a wide range of behaviors and phenomena, from large-scale structures such as active regions, sunspots, and flares, to smaller, quiet Sun structures where interactions at small scales drive the evolution of magnetic flux. This diversity, observable in various spectral lines and across different regions of the solar disk, demands multiple observations with distinct characteristics.

Prior to the first flight of Sunrise III in 2022, a series of timelines were developed to program both calibration and scientific observation blocks. These timelines were carefully designed by the Sunrise Science Team, taking into account the 70 observing proposals submitted for Sunrise, in order to prioritize observations that met the requirements of the majority of these proposals.

Observing proposals that could be fulfilled by targeting the same solar feature, while considering its disk position, were grouped into a single timeline. Each timeline included not only the necessary scientific observation blocks but also the required calibration observations to ensure data accuracy. Thus, timelines consist of a sequence of scientific and calibration observation blocks. The observing blocks within a timeline could vary in content depending on the scientific objectives and the status of the other instruments involved.

For simplicity, operations related to SCIP and SUSI will be excluded from the discussion, save for a few important remarks. In the case of TuMag, each observing block was composed either of a combination of two observing modes executed consecutively, or a single observing mode repeated throughout the block.

The timelines of the Sunrise III observation campaign can be grouped in the following blocks:

- ✿ Quiet Sun observations at disk center (QSDC), as the name implies, focus in regions near the solar disk center that are free from significant solar activity. These timelines typically involve long series of observations aimed at studying the small-scale structure and magnetic flux evolution in the quiet Sun.

There are four distinct timelines in this category: three standard timelines, which employ the nominal observing modes, and a different timeline, the (QSDC_HC). This timeline employs high-cadence variations of the standard observing modes specifically designed to enhance the temporal resolution between images, which is crucial for helioseismology techniques.

- ✿ Sunspot observations (SP) are specifically designed to study sunspots. There are four different timelines for this purpose. Some of these are short programs used to track the same sunspot over multiple days, with the goal of studying the evolution and decay of the sunspot. Others are more extensive programs aimed at examining, in greater detail, the magnetic activity of sunspots and their penumbral structures.
- ✿ Polar observations (PL) target the region close to the limb in both poles of the Sun. These areas are of special interest due to their distinct magnetic behavior compared to the disk center. Additionally, these regions provide the opportunity to measure faint signals outside the main solar disk, such as spicules in the lower chromosphere,

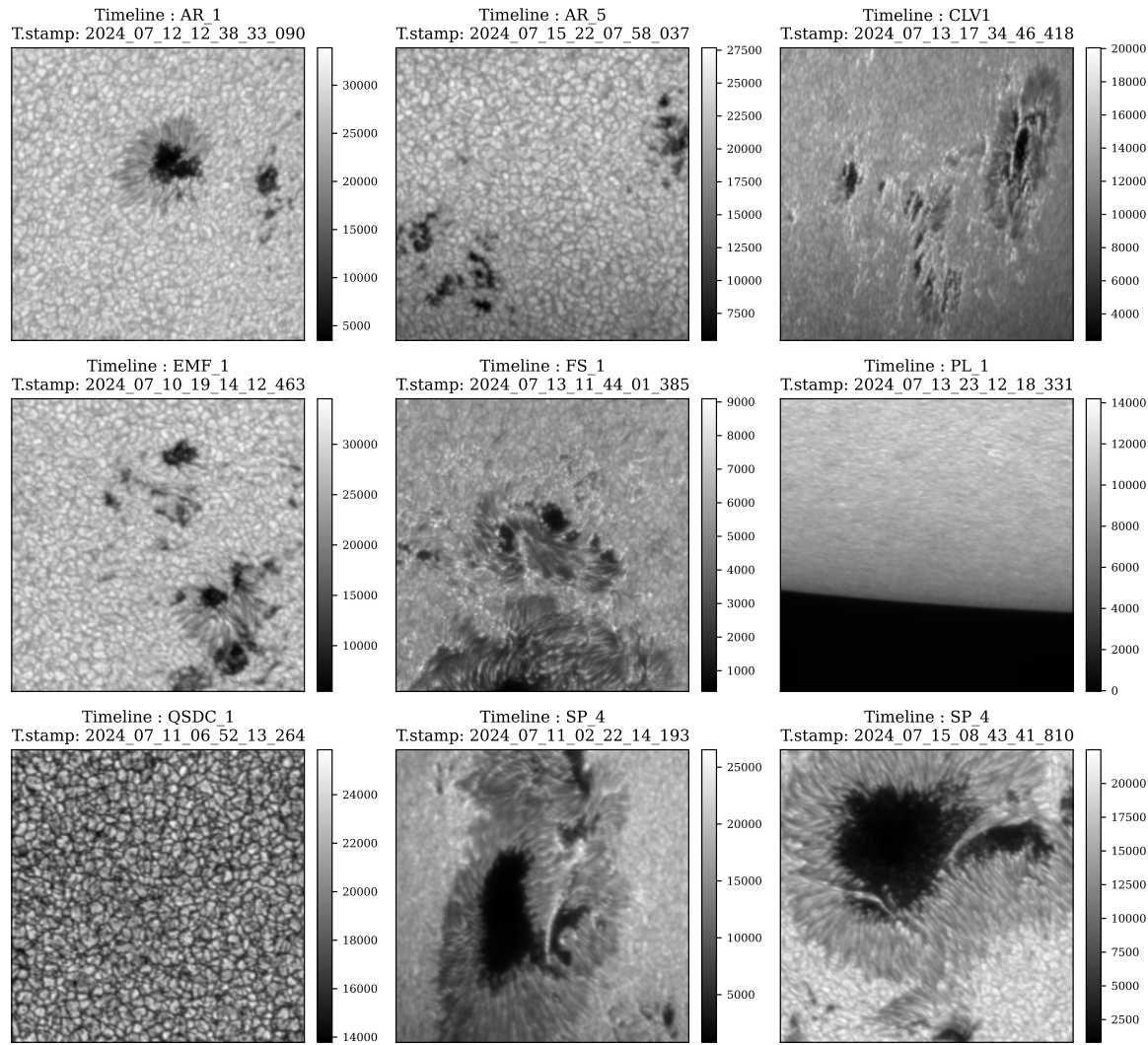


Figure 3.4 Continuum images of the first modulation of the first observation mode from different timelines. The image shown has been flat-fielded and dark-corrected. The timestamp provided corresponds to the first image of the observation mode. The colorbar is given in counts.

observed outside the continuum disk of iron. Two different instances of these timelines are conceived in the observation campaign, mostly differentiated in TuMag by the selected spectral lines.

- East and West limb (EW) observations are designed to target the equatorial regions of the solar limb. In addition to exhibiting magnetic structures distinctly different from those observed at the poles, the reason for having a separate timeline from the PL timelines lies in the orientation and technical constraints related to SCIP and SUSI's slits. The relative positioning of the regions and the inclination of the telescope introduce unique challenges. In these EW observations, the spectrometer slits are aligned parallel to the limb, contrasting with the PL timelines, where the slit is positioned perpendicular to the limb.
- Active regions (AR) observations are designed to study areas exhibiting solar activity, excluding those specifically focused on in the sunspot programs. These observations typically consist of two-hour series, employing the standard combination of the iron 525.02 nm and magnesium lines, using modes 1 and 2.02, which represent the most common observation block for TuMag. Although five different AR timelines were planned for the Sunrise campaign, only three were executed.
- Emergence flux (EMF) programs are specifically designed to study active regions that exhibit a large flux emergence. For TuMag, the observation blocks are shared with those of the AR programs, namely, the combination of mode 1 and 2.02 for series of around 2 hours.
- Full spectral scan (FS) observations are primarily designed for SUSI and SCIP, where their complete set of spectral bands is utilized. These scans are intended to be carried out in both quiet Sun and active regions. For TuMag, FS observations consist of long series focusing on the iron spectral line in quiet Sun regions, while in active regions, they include a combination of iron and magnesium observations.
- The flares programs (FL) were designed for target opportunities of a flaring region. These programs were intended to be activated only when an active region showed signs of flaring. For TuMag, the observations during these programs consist of the standard combination of iron 525.02 nm and magnesium spectral lines.
- Center-to-limb variation (CLV) observations were intended to target regions of the solar disk characterized by μ values that had not been previously observed. The parameter μ , defined as the cosine of the angle between the surface normal and the observer's line of sight, serves as a useful indicator of a region's proximity to the disk center. Specifically, μ ranges from 1 at the disk center to 0 at the limb (Thompson, 2006). Conducting CLV observations at previously unmeasured μ values enables us to capture data from different regions across the disk, facilitating studies of how observational features vary with their position on the disk.

During the Sunrise III observation campaign, 38 timelines were run, including calibration timelines in addition to the scientific programs presented here. Some examples of the different targets employed during the campaign are shown in fig. 3.4. A detailed record of TuMag's observations can be found online both in the pipeline's repository and in TuMag's official data website[†].

3.3 Pipeline

When light traverses any astronomical instrument, the optical components it encounters between the aperture and the detector can alter the light in unintended ways. These modifications give rise to artifacts that must be corrected prior to the scientific exploitation of the observations, as they can falsify the results if left unaddressed. The process of eliminating these spurious effects is typically referred to as data reduction and is specific to each instrument, as different optical elements require different corrections.

As a spectropolarimeter, TuMag's final data product are not *simply* the measured images but the Stokes components of the incoming light, when either modulation scheme is employed. Consequently, TuMag's data pipeline must not only remove all instrumental artifacts but also include the necessary procedures to demodulate the data and derive the Stokes components for each wavelength along the spectral line.

This section presents the software specifically developed for this purpose. The discussion will cover the various steps that data must undergo before becoming science-ready, as well as the tools created to facilitate this process. All codes related to TuMag's pipeline are publicly available in a GitHub repository[‡], and it is important to note that this software is still under development at the time of writing this thesis.

3.3.1 Standard data reduction process.

We have divided the discussion of the pipeline in two sections, the so-called "standard data reduction process" and the extra calibration blocks. The first being all the steps that are mandatory to process an individual observing mode and produce the Stokes components with the most basic corrections. These are the minimal steps to produce data that can start to be analyzed scientifically. The second block is comprised of all the additional corrections and considerations that may or may not be applied to the data, depending on the nature of the observation. While this division may not be entirely accurate, as science-ready data will likely require the application of additional calibrations, such as image reconstruction, for instance, we have adopted it to simplify the discussion of the pipeline.

All data corresponding to an observing mode whose final product consists of the Stokes components of the incoming light (i.e., all nominal modes except for the 0s mode) must follow the standard reduction process. This process is illustrated in the block diagram in

[†]https://www.uv.es/jublanro/tumag_data_test.html

[‡]https://github.com/PabloSGN/TuMags_Reduction_Pipeline

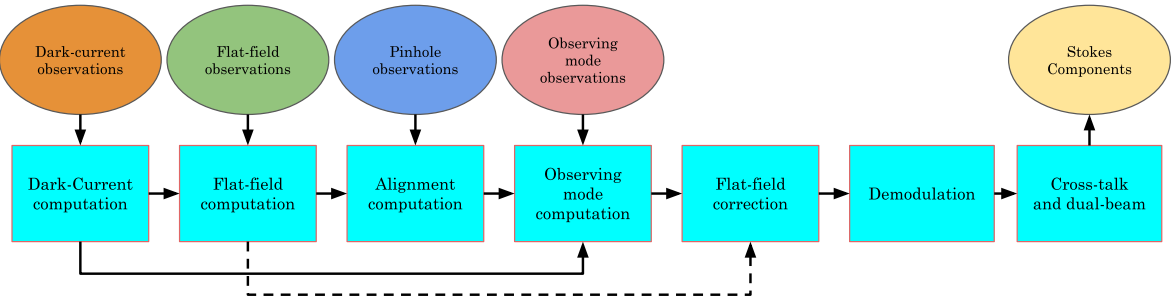


Figure 3.5 Block diagram of the standard reduction process: Blue boxes represent the individual steps that make up the reduction, while ellipses indicate the different sets of observations and the final product (yellow ellipse).

fig. 3.5 and consists of the following steps:

1. Dark current processing.
2. Flat-fielding processing.
3. Camera's alignment computation.
4. Processing of observing mode images (dark-current corrected).
5. Apply flat-field correction.
6. Demodulation.
7. Cross-talk correction and cameras combination.

The data reduction process begins with the dark-current processing, which involves averaging all individual dark frames within a specific set to generate a single dark-current frame per camera. This dark current is then subtracted from all images used in the reduction, including flat-fields, pinholes, and scientific observations, after rescaling the dark-current to the appropriate number of accumulations.

The second step is the flat-field computation. These observations, as previously mentioned, are a modified version of the nominal mode with an increased λ_{rep} and are repeated N_{rep} times. The processing involves averaging all images taken at a specific wavelength for the same modulation. Thus, $\lambda_{\text{rep}} \times N_{\text{rep}}$ images are averaged to produce a single flat-field frame. To maintain spectral line information, flat-fields are normalized to their mean value, as flat-fields taken at the line core have lower intensity than those in the continuum. The goal is to correct intensity variations within a single frame without altering relative intensities across different spectral points.

Since TuMag operates in a dual-beam configuration, data from both cameras must be combined during processing. However, the images from each camera are not initially aligned. To determine the camera alignment, a two-dimensional cross-correlation is performed using the pinhole target from both cameras. Additionally, the field stop position

is required for alignment, as TuMag's detectors are larger than its FoV. A specific function identifies the field stop positions from the processed flat-fields, marking the boundary between dark pixels and those within TuMag's FoV. Figure XX provides a representation of both the pinhole alignment and the field-stop finder.

Having computed the dark-current and the flat-fields, the scientific observations can be corrected by subtracting the dark-current and dividing the resulting image by the flat-field of the corresponding wavelength and modulation.

With the dark-corrected and flat-fielded observations, the stokes components can be computed. The demodulation is carried at each wavelength separately and consists on the matrix multiplication of the demodulation matrix and the four stokes components:

$$\begin{pmatrix} I \\ Q \\ U \\ V \end{pmatrix} = \underbrace{\begin{pmatrix} d_{00} & d_{01} & d_{02} & d_{03} \\ d_{10} & d_{11} & d_{12} & d_{13} \\ d_{20} & d_{21} & d_{22} & d_{23} \\ d_{30} & d_{31} & d_{32} & d_{33} \end{pmatrix}}_{\mathbf{D}} \begin{pmatrix} I_1 \\ I_2 \\ I_3 \\ I_4 \end{pmatrix}, \quad (3.1)$$

Modo Longitudinal?? where the matrix D is the inverse of the modulation matrix of the corresponding camera and pre-filter that were computed during the calibrations (see sec. 2.2.2.3).

From the matrix multiplication the stokes components for each camera are derived. However, the demodulation is never perfect, due to small deviations of the demodulation matrix from the real one, or instrumental artifacts that have been uncorrected by the flat-fielding. These defects result in a contaminated stokes components, where information from one component appears in other components, typically from Stokes I into Q, U, and or V. Nonetheless, these contamination, known as cross-talk, can be extracted from the data.

The cross-talk correction is a manual process since different data sets require different corrections. For instance, some data sets may not show contamination from I to U while others do. Moreover, the correction might require to be applied using the information from the whole FoV or only of a small region. Thus, this is a correction that has to be carefully applied and its hard to standarize to the whole set of observations. However, the concept of the correction is the same.

The correction of the cross-talk from I to any other component starts by measuring the relation between the two components by fitting through a least-squares method, a polynomial of first order in order to compute the tendency, if there is one. Once this relation has been established, and the strength of the cross-talk (*i.e.* the value of the slope) measured, the correction is applied by simply, removing the tendency of the data:

$$S_{corr} = S_{orig} - (I_{orig} * a + b), \quad (3.2)$$

where the relation between the stokes component S_{orig} and stokes I I_{orig} has been fitted to the line: $S_{orig} = I_{orig} * a + b$

3.3.2 Extra calibration blocks.

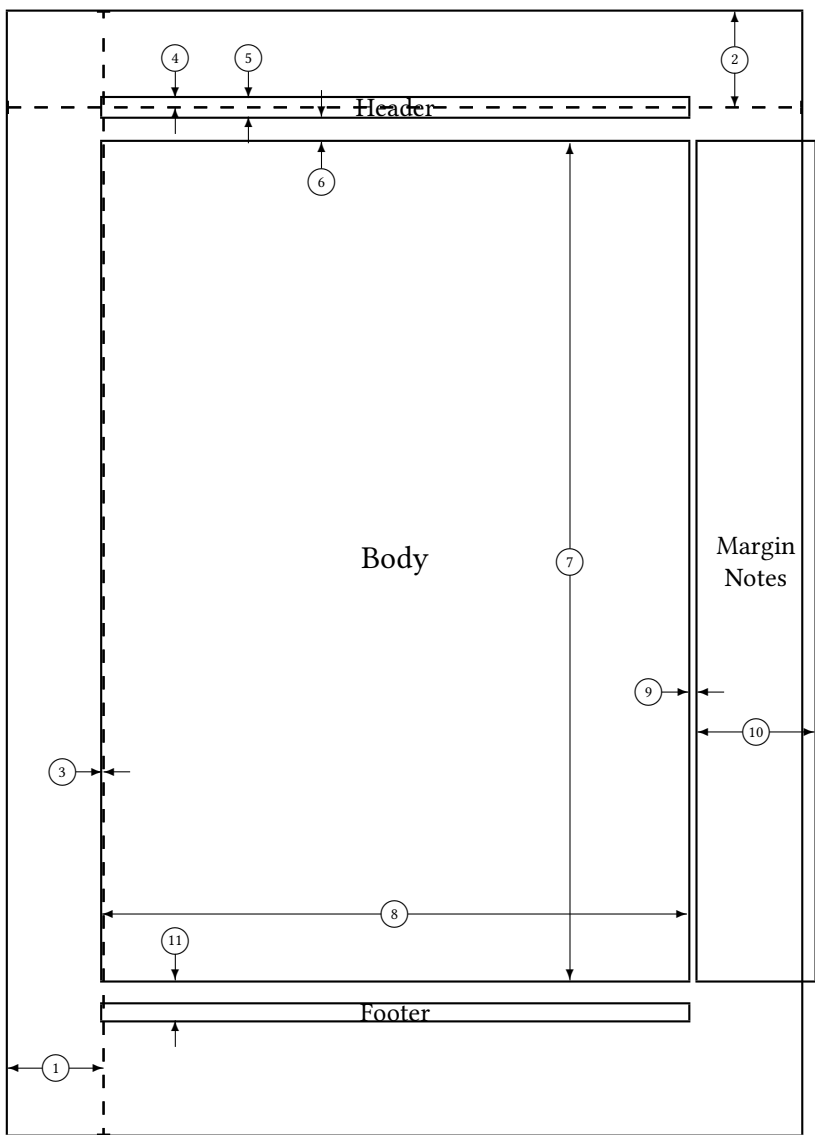
BIBLIOGRAPHY

- Álvarez-Herrero, A., Belenguer, T., Pastor, C., et al. Lithium niobate fabry-perot etalons in double-pass configuration for spectral filtering in the visible imager magnetograph imax for the sunrise mission. *Space Telescopes and Instrumentation I: Optical, Infrared, and Millimeter*, SPIE, 797–812 (2006).
- Álvarez-Herrero, A., Parejo, P. G., & Silva-López, M. Fine tuning method for optimization of liquid crystal based polarimeters. *Optics Express* **26**, 12038 (2018).
- Álvarez-Herrero, A., Parejo, P. G., & Silva-López, M. Fine tuning method for optimization of liquid crystal based polarimeters. *Optics Express* **26**, 12038 (2018).
- Álvarez Herrero, A., Garranzo-García, D., Núñez, A., et al. End-to-end tests of the tumag instrument for the sunrise iii mission. *Ground-based and Airborne Instrumentation for Astronomy IX*, SPIE, 791–802 (2022).
- Bailén, F. J., Orozco Suárez, D., Blanco Rodríguez, J., & del Toro Iniesta, J. C. Performance of Sequential Phase Diversity with Dynamical Solar Scenes. *Astrophys. J. Suppl.* **263**, 7 (2022).
- Bailén, F. J., Suárez, D. O., & del Toro Iniesta, J. On fabry–pérot etalon-based instruments. i. the isotropic case. *The Astrophysical Journal Supplement Series* **241**, 9 (2019).
- Barthol, P., Gandorfer, A., Solanki, S. K., et al. The sunrise mission. *Solar Physics* **268**, 1 (2011).
- Bellot Rubio, L., & Orozco Suárez, D. Quiet sun magnetic fields: an observational view. *Living Reviews in Solar Physics* **16**, 1 (2019).
- Bianda, M., Solanki, S., & Stenflo, J. Hanle depolarisation in the solar chromosphere. *Astronomy and Astrophysics*, v. 331, p. 760-770 (1998) **331**, 760 (1998).
- Childlaw, R., Devaney, A., & Gonsalves, R. Analytical studies of phase estimation techniques, volume 1. *Final Technical Report* (1979).
- Danilovic, S., Beeck, B., Pietarila, A., et al. Transverse component of the magnetic field in the solar photosphere observed by sunrise. *The Astrophysical Journal Letters* **723**, L149 (2010).

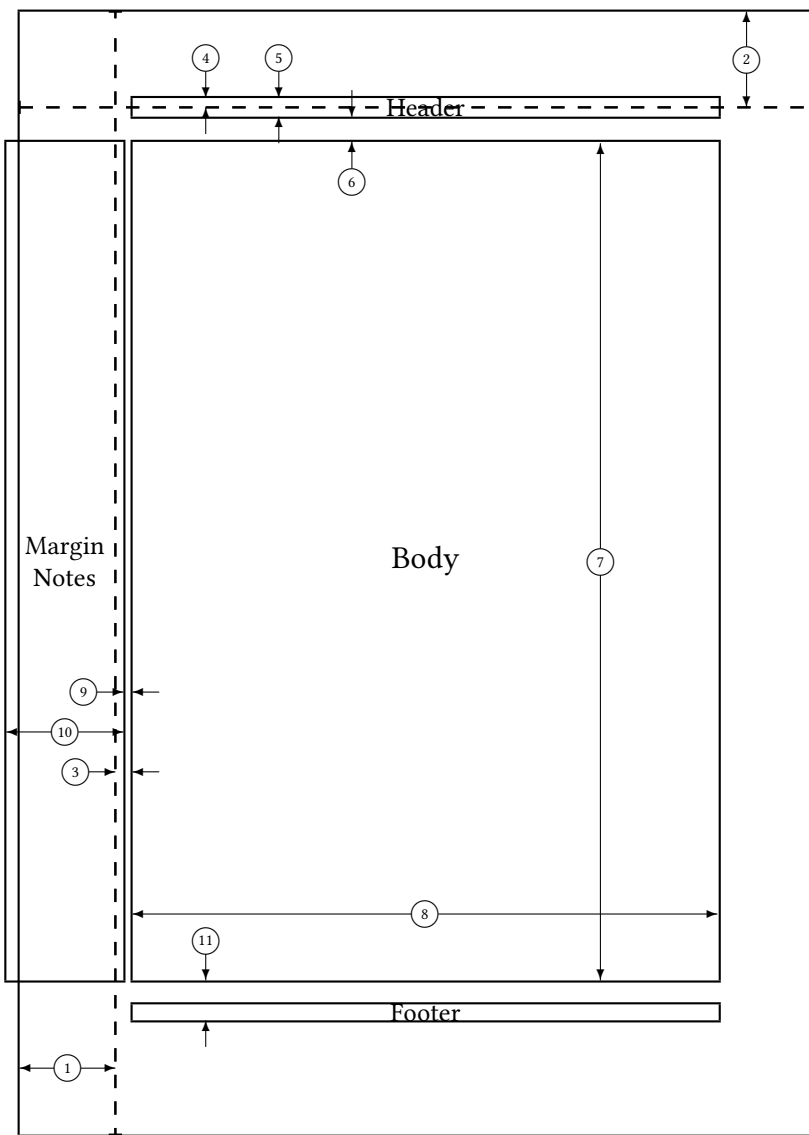
- del Toro Iniesta, J. C. (2003), Introduction to spectropolarimetry (Cambridge university press).
- del Toro Iniesta, J. C., & Collados, M. Optimum modulation and demodulation matrices for solar polarimetry. *Applied Optics* **39**, 1637 (2000).
- del Toro Iniesta, J. C., & Ruiz Cobo, B. Inversion of the radiative transfer equation for polarized light. *Living Reviews in Solar Physics* **13**, 4 (2016).
- Elmore, D. F., Lites, B. W., Tomczyk, S., et al. Advanced stokes polarimeter: a new instrument for solar magnetic field research. *Polarization analysis and measurement*, SPIE, 22–33 (1992).
- Gaskill, J. D. (1978), Linear systems, Fourier transforms, and optics, Vol. 56 (John Wiley & Sons).
- Gizon, L., Birch, A. C., & Spruit, H. C. Local helioseismology: three-dimensional imaging of the solar interior. *Annual Review of Astronomy and Astrophysics* **48**, 289 (2010).
- González, N. B., & Kneer, F. Narrow-band full stokes polarimetry of small structures on the sun with speckle methods. *Astronomy & Astrophysics* **480**, 265 (2008).
- Guglielmino, S., Pillet, V. M., Bonet, J., et al. The frontier between small-scale dipoles and ephemeral regions in the solar photosphere: emergence and decay of an intermediate-scale dipole observed with sunrise/imax. *The Astrophysical Journal* **745**, 160 (2012).
- Helstrom, C. W. Image restoration by the method of least squares. *Josa* **57**, 297 (1967).
- Hotta, H., Rempel, M., & Yokoyama, T. Efficient small-scale dynamo in the solar convection zone. *The Astrophysical Journal* **803**, 42 (2015).
- Huang, K.-Y., Chia, C.-M., & Chang, E. Optical resolution measurement system for small lens by using slanted-slit method. *Optical Measurement Systems for Industrial Inspection VIII*, SPIE, 705–712 (2013).
- Kosugi, T., Matsuzaki, K., Sakao, T., et al. The hinode (solar-b) mission: An overview. *Solar Physics* **1**, 3 (2007).
- Lakshminarayanan, V., & Fleck, A. Zernike polynomials: a guide. *Journal of Modern Optics* **58**, 545 (2011).
- Lites, B., Elmore, D., & Streander, K. The solar-b spectro-polarimeter. *Advanced solar polarimetry—theory, observation, and instrumentation*, 33 (2001).
- Lites, B. W. Rotating waveplates as polarization modulators for stokes polarimetry of the sun: evaluation of seeing-induced crosstalk errors. *Applied Optics* **26**, 3838 (1987).

- Martínez Pillet, V., Collados, M., Sánchez Almeida, J., et al. Lpsp & tip: full stokes polarimeters for the canary islands observatories. *High Resolution Solar Physics: Theory, Observations, and Techniques*, 264 (1999).
- Müller, D., Cyr, O. S., Zouganelis, I., et al. The solar orbiter mission-science overview. *Astronomy & Astrophysics* **642**, A1 (2020).
- Orozco Suárez, D., Álvarez García, D., López Jiménez, A. C., et al. Spgcam: A specifically tailored camera for solar observations. *Frontiers in Astronomy and Space Sciences* **10**, 1167540 (2023).
- Parker, E. Magnetic neutral sheets in evolving fields-part two-formation of the solar corona. *Astrophysical Journal, Vol. 264, P. 642, 1983* **264**, 642 (1983).
- Paxman, R. G., Schulz, T. J., & Fienup, J. R. Joint estimation of object and aberrations by using phase diversity. *JOSA A* **9**, 1072 (1992).
- Petrovay, K., & Szakaly, G. The origin of intranetwork fields: a small-scale solar dynamo. *Astronomy and Astrophysics, Vol. 274, p. 543 (1993)* **274**, 543 (1993).
- Pillet, V. M., Bonet, J. A., Collados, M. V., et al. The imaging magnetograph experiment for the sunrise balloon antarctica project. *Optical, Infrared, and Millimeter Space Telescopes*, SPIE, 1152–1164 (2004).
- Pontin, D. I., & Hornig, G. The parker problem: existence of smooth force-free fields and coronal heating. *Living Reviews in Solar Physics* **17**, 5 (2020).
- Rempel, M., Bhatia, T., Bellot Rubio, L., & Korpi-Lagg, M. J. Small-scale dynamos: from idealized models to solar and stellar applications. *Space Science Reviews* **219**, 36 (2023).
- Sánchez, A., Gonzalo, A., Garranzo, D., et al. High precision and thermally controlled filter wheel. *Advances in Optical and Mechanical Technologies for Telescopes and Instrumentation V*, SPIE, 1120–1135 (2022).
- Scharmer, G. Comments on the optimization of high resolution fabry-pérot filtergraphs. *Astronomy & Astrophysics* **447**, 1111 (2006).
- Shibata, K., Nakamura, T., Matsumoto, T., et al. Chromospheric anemone jets as evidence of ubiquitous reconnection. *Science* **318**, 1591 (2007).
- Snyder, A. W. (1975), in Photoreceptor optics (Springer), 38–55.
- Solanki, S., Riethmüller, T., Barthol, P., et al. The second flight of the sunrise balloon-borne solar observatory: overview of instrument updates, the flight, the data, and first results. *The Astrophysical Journal Supplement Series* **229**, 2 (2017).
- Solanki, S. K., del Toro Iniesta, J., Woch, J., et al. The polarimetric and helioseismic imager on solar orbiter. *Astronomy & Astrophysics* **642**, A11 (2020).

- Stokes, G. G. On the composition and resolution of streams of polarized light from different sources. *Transactions of the Cambridge Philosophical Society* **9**, 399 (1851).
- Thompson, W. Coordinate systems for solar image data. *Astronomy & Astrophysics* **449**, 791 (2006).
- Tsuneta, S., Ichimoto, K., Katsukawa, Y., et al. The solar optical telescope for the hinode mission: an overview. *Solar Physics* **249**, 167 (2008).
- Tyson, R. K. (2000), Introduction to adaptive optics, Vol. 41 (SPIE press).
- Uitenbroek, H. The accuracy of the center-of-gravity method for measuring velocity and magnetic field strength in the solar photosphere. *The Astrophysical Journal* **592**, 1225 (2003).
- Van Noort, M., & van der Voort, L. R. Stokes imaging polarimetry using image restoration at the swedish 1-m solar telescope. *Astronomy & Astrophysics* **489**, 429 (2008).
- Vargas Dominguez, S. Study of horizontal flows in solar active regions based on high-resolution image reconstruction techniques. *Ph. D. Thesis* (2009).
- Vargas Dominguez, S. Study of horizontal flows in solar active regions based on high-resolution image reconstruction techniques. *Ph. D. Thesis* (2009).
- Wedemeyer-Böhm, S., Scullion, E., Steiner, O., et al. Magnetic tornadoes as energy channels into the solar corona. *Nature* **486**, 505 (2012).
- Zernike, F. Diffraction theory of the knife-edge test and its improved form, the phase-contrast method. *Monthly Notices of the Royal Astronomical Society*, Vol. 94, p. 377-384 **94**, 377 (1934).
- Zwaan, C. Elements and patterns in the solar magnetic field. IN: *Annual review of astronomy and astrophysics. Volume 25 (A88-13240 03-90)*. Palo Alto, CA, Annual Reviews, Inc., 1987, p. 83-111. **25**, 83 (1987).



1 one inch + \hoffset	2 one inch + \voffset
3 \oddsidemargin = -1pt	4 \topmargin = -7pt
5 \headheight = 14pt	6 \headsep = 19pt
7 \textheight = 631pt	8 \textwidth = 441pt
9 \marginparsep = 7pt	10 \marginparwidth = 88pt
11 \footskip = 30pt	\marginparpush = 7pt (not shown)
\hoffset = 0pt	\voffset = 0pt
\paperwidth = 597pt	\paperheight = 845pt



1 one inch + \hoffset	2 one inch + \voffset
3 \evensidemargin = 13pt	4 \topmargin = -7pt
5 \headheight = 14pt	6 \headsep = 19pt
7 \textheight = 631pt	8 \textwidth = 441pt
9 \marginparsep = 7pt	10 \marginparwidth = 88pt
11 \footskip = 30pt	\marginparpush = 7pt (not shown)
\hoffset = 0pt	\voffset = 0pt
\paperwidth = 597pt	\paperheight = 845pt